Things we need for the proposal:

1. Need plot of projected FF data points as a function of Q^2 integrated over t. Include on the plot the PrimEx-II data point, and the CELLO and BESIII FF points (Ilya)

2. Provide write up on "Results from fitting pseudo-data: projected sensitivities". If the fit error for $\Gamma_{\pi^0 \to \gamma\gamma}$ is less than the PrimEx uncertainty, this indicates sensitivity to $\Gamma_{\pi^0 \to \gamma\gamma}$ comparable to or better than PrimEx. (Ilya)

3. If it seems feasible to determine $\Gamma_{\pi^0 \to \gamma\gamma}$ in the TFF measurement, then indicate how we can do this: (i) measure absolute cross sections or (ii) measure cross sections normalized to a known QED reaction (Moller?), or (iii) say that we're going to do both. Provide write up on the details. (Ilya, ...)

4. Based on the estimated experimental uncertainties in $\Gamma_{\pi^0 \to \gamma\gamma}$, a_π, b_π and c_π, estimate the uncertainty in $a_\mu^{HLbL-\pi^0}$ (Rory)

5. Update section on "Summary of the proposed experiment and impact on studies of fundamental symmetries" (Ilya and Rory)

6. Need write up on Sergey's nuclear coherent π^0 electro-production calculation. Can start with the page he provided us. (Sergey)

7. Do a careful read through. (all)

Proposal to PAC 50

Measurement of the Neutral Pion Transition Form Factor

D. Dale[1], D. Dutta[2], A. Fabrizi[6], L. Gan[3], A. Gasparian[4], S. Gevorkyan[5], I. Larin[6,†], N. Liyanage[7], R. Miskimen[6], A. Schick[6], G. Turnberg[6]

[1] Idaho State University, Pocatello, ID 83209
[2]Mississippi State University, Mississippi State, MS 39762
3 University of North Carolina Wilmington, Wilmington, NC 28403
[4] North Carolina A&T State University, Greensboro, NC 27411
[5] Joint Institute for Nuclear Research, Dubna, Russia 141980
[6] University of Massachusetts, Amherst MA 01003
[7]University of Virginia, Charlottessville, VA 22904

June 22, 2022

† Contact person

Abstract

We propose a measurement of the π^0 space-like transition form factor (TFF) through the Primakoff reaction with virtual incident photons. The experiment will run using the PRad setup in Hall B using $100\,\mu$ and $250\,\mu m$ thick silicon targets, and a 10.5 GeV electron beam with 20 nA and 10 nA current. The measurement has sensitivity to two fundamental observables in low-energy, strong-interaction physics, (i) the π^0 radiative decay width $\Gamma_{\pi^0\to\gamma\gamma}$, and (ii) the π^0 electromagnetic transition radius. The measurement will determine $\Gamma_{\pi^0\to\gamma\gamma}$ with an estimated uncertainty of $\pm\,0.9(yy)\,\%$ stat. (sys.), to be compared with the combined PrimEx-I and PrimEx-II result of $\pm\,0.7(1.3)\,\%$ [1]. One of the larger uncertainties in the Standard Model prediction for the muon anomalous magnetic moment is hadronic light-by-light scattering (HLbL), which critically depends on knowledge of the pseudo-scalar meson TFFs in the low-Q^2 region. By measuring the π^0 TFF over the region $Q^2 \approx .003$ to $0.3\,\text{GeV}^2$, where no data currently exists, the proposed experiment will constrain approximately 65 % of the π^0-pole contribution to HLbL with an estimated uncertainty of zz %.

1 Introduction and physics motivation

The neutral pion transition form factor (TFF) in the low-Q^2 space-like region can determine two key observables in low-energy strong-interaction physics, the neutral pion radiative width $\Gamma_{\pi^0\to\gamma\gamma}$, and the neutral pion transition radius. These observables provide important test points for calculations based on fundamental symmetries and chiral perturbation theory, [2], as well as providing important constraints for hadronic corrections to the muon anamalous magnetic moment [3, 4].

Primakoff π^0 electro-production can be used to measure the space-like π^0 electromagnetic TFF. Fig. 1 shows the Feynman diagram for the interaction vertex. We define Q_1^2 as the negative 4-momentum transfer squared from the electron vertex, and Q_2^2 as the corresponding quantity from the nuclear vertex, where $Q_2^2 = -t$ in terms of the usual Mandelstam variable. The transition is characterized by the form factor $F_{\gamma^*\gamma^*\to\pi^0}(-Q_1^2, -Q_2^2)$, which to order $O(Q^4)$ is given by,

$$F_{\gamma^*\gamma^*\to\pi^0}(-Q_1^2,-Q_2^2) = \sqrt{\frac{4\Gamma_{\pi^0\to\gamma\gamma}}{\pi\alpha^2 m_\pi^3}}\left[1-\frac{a_\pi}{m_\pi^2}\left(Q_1^2+Q_2^2\right)+\frac{b_\pi}{m_\pi^4}\left(Q_1^4+Q_2^4\right)+\frac{c_\pi}{m_\pi^4}Q_1^2Q_2^2+...\right] \quad (1)$$

where a_π and b_π are the linear and curvature terms in the TFF, respectively, and c_π is a cross term in the expansion.

The cross section for virtual Primakoff production has been given by Hadjimichael and Fallieros [5],

$$\begin{aligned}\frac{d^3\sigma_P}{dE_2 d\Omega_2 d\Omega_\pi} &= \frac{Z^2\eta^2}{\pi}\sigma_M \frac{k_\pi^4}{t^2}\frac{\beta_\pi^{-1}}{E_\pi}\left|F_N(t)\right|^2 \left|\frac{F_{\gamma^*\gamma^*\to\pi^o}(-Q^2,t)}{F_{\gamma^*\gamma^*\to\pi^o}(0,0)}\right|^2 sin^2(\frac{\theta_e}{2})sin^2(\theta_\pi) \\ &\times\left[4E_1E_2 sin^2\phi_\pi + |\vec{q}|^2/cos^2(\frac{\theta_e}{2})\right]\end{aligned} \quad (2)$$

where σ_M the Mott cross section and η are given by,

$$\sigma_M = \frac{\alpha^2 cos^2(\frac{\theta_e}{2})}{4E_1^2 sin^4(\frac{\theta_e}{2})} \quad (3)$$

$$\eta^2 = \frac{4}{\pi m_\pi^3}\Gamma_{\pi^0\to\gamma\gamma} \quad (4)$$

and $F_N(t)$ is the nuclear form factor, θ_e is the electron scattering angle, and θ_π is the angle between the virtual photon beam momentum $\vec{q}$ direction and the neutral pion momentum $\vec{k}_\pi$ direction. This expression for the cross section in similar to that for the real Primakoff effect, with the notable exception of the form factor $F_{\gamma^*\gamma^*\to\pi^0}(-Q^2,t)$ which is of interest here.

The $\gamma^*\gamma^*\pi^0$ vertex has been studied theoretically in VMD and ChPT based models, [6, 7, 8], as well as those based on treatments of quark substructure [9, 10, 11]. In light of the recent result for muon $g-2$, there has been considerable theoretical interest in the pseudo-scalar TFFs and how they impact hadronic corrections to $(g-2)_\mu$ (see discussion in section 2). Most recently lattice calculations [12, 13] have been developed with sufficient accuracy to complement and test predictions for $(g-2)_\mu$ from analytical approaches.

The most significant background to consider in Primakoff experiments is π^0 coherent photo-production [1]. Fig. 2 shows a "textbook" example of this from the PrimEx-II ^{28}Si data. The prominent peak at the lowest angle is from the Primakoff reaction, and the peak at $\approx 1.3^o$ is the coherent background. The methodology for extracting the Primakoff signal from the coherent and incoherent backgrounds is well established [1]. In brief, the shapes of the Primakoff and coherent angular distributions are constrained, the former by QED and the nuclear electromagnetic form factor, and the latter by the t-dependence of the "strong" nuclear form factor and the pion-nucleus interaction. The strong nuclear form factor is ... Therefore, the analysis effectively reduces to fitting the π^0 angular distribution with the squared sum of the Primakoff and coherent amplitudes, with the coherent amplitude multiplied by an arbitrary complex phase. The complex phase accounts for the phase difference between the Coulomb amplitude (Primakoff), and the strong amplitude (coherent).

In support of this proposal S. Gevorkyan, our PrimEx theoretical collaborator, is developing a generalization of the coherent amplitude for the case of electro-production. This work is in progress, and details of the calculation are given in Appendix A. In the low-Q^2 range of the TFF measurement it can be reasonably assumed that the photo- and electro-production coherent angular distributions (the former is shown in Fig. 2 for ^{28}Si) are similar. For the TFF measurement we plan to take data on a ^{28}Si target.

Finally, we note that a proposal to measure the pseudo-scalar TFFs was developed by the PrimEx Collaboration over 20 years ago. The proposal was included in the original JLab white paper as a key experiment driving the 12 GeV energy upgrade [14, 15].

2 Hadronic corrections to the muon anomalous magnetic moment

Recently there has been considerable interest in measurements of the pseudo-scalar meson TFFs as a means to constrain hadronic corrections to the muon anomalous magnetic moment. Defining $a_\mu = (g-2)_\mu/2$ as the deviation of the magnetic moment from the value g=2 for a point-like spin-1/2 Dirac particle, the experimental measurement [16] and Standard Model (SM) prediction [4] for a_μ are given by,

$$a_\mu^{exp} = 116\ 592\ 061\ (41) \times 10^{-11} \tag{5}$$

$$a_\mu^{SM} = 116\ 591\ 810\ (43) \times 10^{-11} \tag{6}$$

which gives a 4.2σ deviation between experiment and Standard Model. As of this writing FNAL E989 continues to take data on $(g-2)_\mu$, with data taking planned at J-PARC in

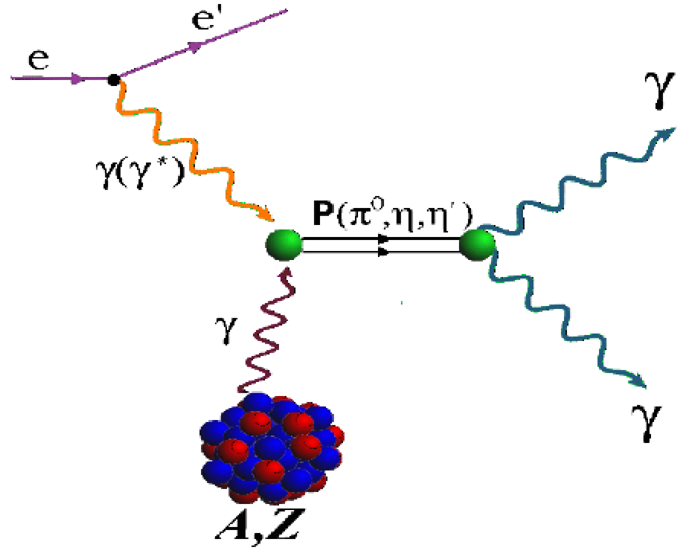

Figure 1: Feynman diagram for the virtual Primakoff reaction

the near future. Therefore, it is reasonable to expect there will be a significant reduction in the experimental error in a_μ over the next several years. For this reason comprehensive theoretical **and experimental efforts** are underway to reduce the Standard Model uncertainty in a_μ.

There are four classes of corrections to the SM prediction for a_μ^{SM}: (i) higher-level QED diagrams to order α^{12}, (ii) electro-weak corrections at 3-loop level, (iii) hadronic vacuum polarization, and (iv) hadronic light-by-light scattering. Theoretical uncertainties in the first two processes, QED and electro-weak corrections, are understood to be small, $\pm 1 \times 10^{-12}$ and $\pm 1 \times 10^{-11}$, respectively, and do not limit the interpretation of the experimental results [4].

The third class of correction, hadronic vacuum polarization HVP, can be calculated using data driven techniques using experimental data. In the data-driven approach the lowest order HVP is given by $\int K(s)R(s)/s^2\, ds$, where $\sqrt{s}$ is the C.M. energy of the e^+e^- system, K(s) is a known kinematic factor, and R(s) is given by,

$$R(s) = \frac{\sigma(e^+e^- \to hadrons)}{\sigma(e^+e^- \to \mu^+\mu^-)} \tag{7}$$

The evaluation of HVP currently stands at $a_\mu^{HVP} = 6845 \pm 40 \times 10^{-11}$ [4]. As new measurements of $e^+e^- \to X$ improve the determination of R, the error in HVP is expected to significantly decrease.

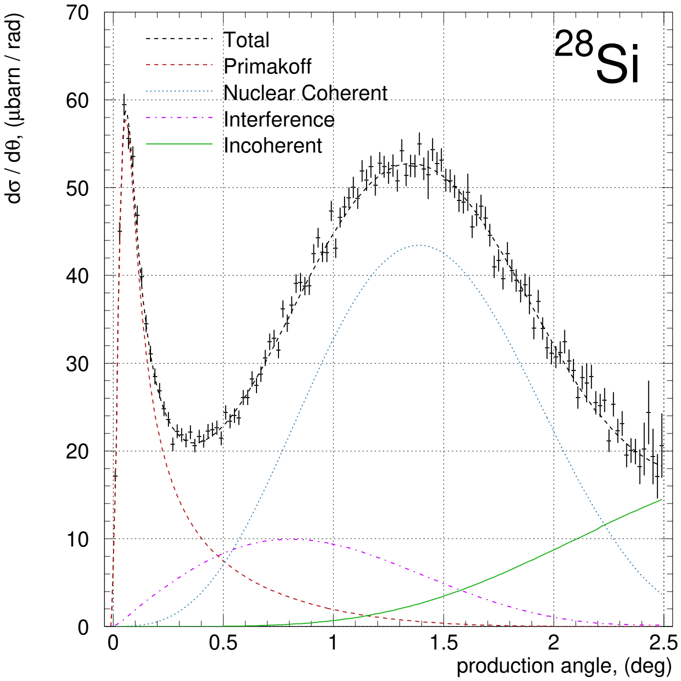

Figure 2: ^{28}Si data from the PrimEx-II analysis. The curves show the Primakoff signal (brown), and the coherent (blue), interference (magenta) and incoherent (green) backgrounds.

The fourth class of correction, and arguably the most model-dependent in its evaluation, is hadronic light-by-light scattering, HLbL. Since HLbL is suppressed by a factor α relative to HVP, a_μ^{HLbL} is roughly two orders of magnitude smaller than a_μ^{HVP}. Unlike HVP, HLbL cannot be reduced to purely data-driven forms, and must be evaluated using experimental data and hadronic models [3, 4]. The evaluation of HLbL currently stands at $a_\mu^{HLbL} = 92 \pm 19 \times 10^{-11}$ [4]. While a_μ^{HLbL} is much smaller than a_μ^{HVP}, with $a_\mu^{HLbL} \approx \alpha \times a_\mu^{HVP}$, *the uncertainties in HLbL and HVP are of comparable size.*

The single largest contribution to HLbL is from the coupling of two space-like photons to the pseudo-scalar mesons π^0, η and η', with the coupling parameterized by the pseudo-scalar TFFs. TFF data are used as input for the evaluation of the pseudo-scalar pole contributions to HLbL, and for the validation of hadronic models used to calculate the TFFs. Evaluation of the pseudo-scalar pole contribution to HLbL currently stands at $a_\mu^{HLbL-pole} = 93.8 \pm 4.0 \times 10^{-11}$ [4], equal within errors to the total for HLbL summed over all contributions, $a_\mu^{HLbL} = 92 \pm 19 \times 10^{-11}$. Due to the low mass of the π^0 relative to the η and η', approximately 67% of $a_\mu^{HLbL-pole}$ comes from the π^0-pole.

Details for calculating $a_\mu^{HLbL-pole}$ are presented in Appendix A. Also presented in the appendix are the computational tools we've used for the evaluation of $a_\mu^{HLbL-\pi^0}$. The expression for $a_\mu^{HLbL-\pi^0}$ is given by the following equation, [17]

$$a_\mu^{HLbL-\pi^0} = \left(\frac{\alpha}{\pi}\right)\left[a_\mu^{\mathrm{HLbL:}\pi^0(1)} + a_\mu^{\mathrm{HLbL:}\pi^0(2)}\right] \tag{8}$$

where the two terms on the right must be evaluated from triple integrals over the TFFs,

$$a_\mu^{\mathrm{HLbL:}\pi^0(1)} = \int_0^\infty dQ_1 \int_0^\infty dQ_2 \int_{-1}^1 d\tau w_1(Q_1, Q_2, \tau)\mathcal{F}_{\pi^0\gamma^*\gamma^*}(-Q_1^2, -(Q_1+Q_2)^2)\mathcal{F}_{\pi^0\gamma^*\gamma^*}(-Q_2^2, 0) \tag{9}$$

$$a_\mu^{\mathrm{HLbL:}\pi^0(2)} = \int_0^\infty dQ_1 \int_0^\infty dQ_2 \int_{-1}^1 d\tau w_2(Q_1, Q_2, \tau)\mathcal{F}_{\pi^0\gamma^*\gamma^*}(-Q_1^2, -Q_2^2)\mathcal{F}_{\pi^0\gamma^*\gamma^*}(-(Q_1+Q_2)^2, 0) \tag{10}$$

with $Q_1 = \sqrt{Q_1^2}$ and $Q_2 = \sqrt{Q_2^2}$, and where w_1 and w_2 are weighting functions given in Appendix A.

Fig. 3 shows $a_\mu^{HLbL-\pi^0}$ as a fraction of the asymptotic value versus the momentum cutoff used for the integrals in Eqns. 9 and 10. The figure indicates that $a_\mu^{HLbL-\pi^0}$ saturates with increasing momentum cutoff. At a momentum cutoff of 0.55 GeV, corresponding to $Q^2 = 0.3\ GeV^2$, $a_\mu^{HLbL-\pi^0}$ is at 65 % of the asymptotic value.

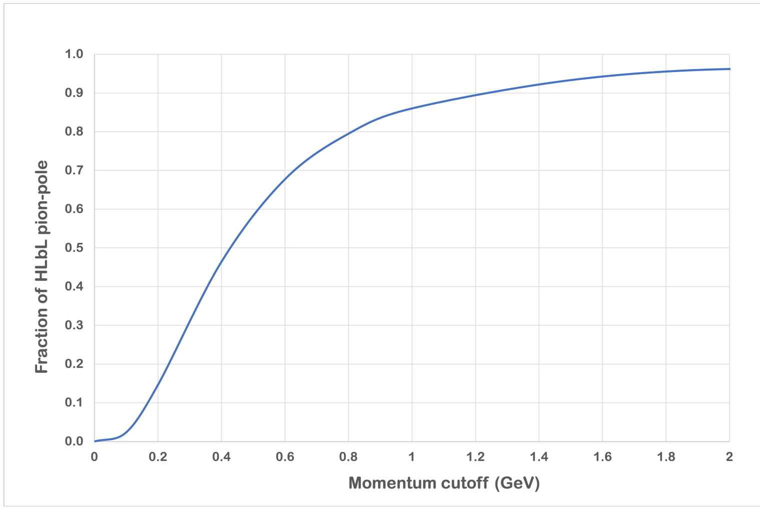

Figure 3: $a_\mu^{HLbL-\pi^0}$ as a fraction of the asymptotic value as a function of the momentum cut-off.

3 Previous Measurements of the Neutral Pion TFF in the space-like region

There are three sources of data for the π^0 TFF in the low-Q^2 space-like region. Arguably the most important data point is the radiative width of the neutral pion, $\Gamma_{\pi^0\to\gamma\gamma}$, which fixes the normalization of $F_{\gamma^*\gamma^*\to\pi^0}(0,0)$. Results for the π^0 radiative width were recently published in *Science* [1]. Combining the PrimEx-I and PrimEx-II results gives

$$\Gamma_{\pi^0\to\gamma\gamma} = 7.802 \pm 0.052(stat) \pm 0.105(sys)\ eV$$

Experimental results for $\Gamma_{\pi^0\to\gamma\gamma}$ from PrimEx and previous measurements are shown in Fig. 4. The PrimEx result is in agreement with the Chiral Anomaly prediction, and deviates from theoretical corrections to the anomaly by two standard deviations.

The second source of data are from collider measurements, where $\gamma^*\gamma \to \pi^0$. The lowest Q^2 published measurements are by CELLO [18] and CLEO [19] in the Q^2 ranges 0.6-2.2 GeV^2 and 1.6-8.0 GeV^2, respectively. These measurements used the reaction $e^+e^- \to e^+e^-\pi^0$, where two photons are radiated by the colliding e^+e^- beams, one photon close to real and the second virtual, followed by $\gamma^*\gamma \to \pi^0$. Tagging either the e^+ or e^- allows for the determination of Q^2. There are also preliminary data from BESIII covering the range from 0.3 to 3.1 GeV^2 [20]. Calculation of the radiative correction for the BESIII efficiencies is currently in progress. Fig. 5 shows low-Q^2 data collected to date on the spacelike π^0 TFF.

The third source of data are from the Dalitz decay $\pi^0 \to e^+e^-\gamma$. Although the Dalitz decay probes the time-like region of the TFF, the "slope" of the yield relative to e^+e^-

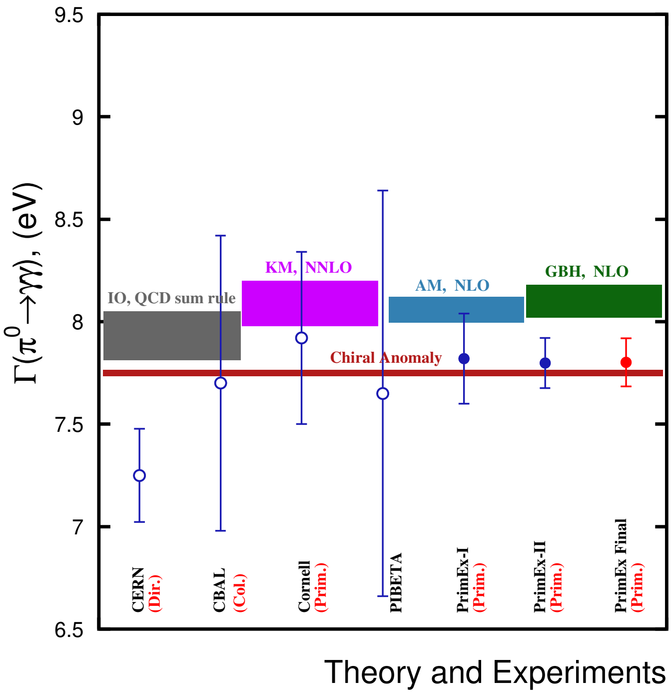

Figure 4: Measurements and calculations for the neutral pion radiative width.

invariant mass-squared is sensitive to the slope term a_π in Eqn. 1 In the low-q^2 limit the TFF is proportional to,

$$F(x) \propto 1 + a_\pi x$$

where

$$x = \frac{m^2_{e^+e^-}}{m^2_\pi}$$

The most recent π^0 Dalitz decay measurements are from NA62 [21], an analysis of approximately 1.1 M reconstructed Dalitz decays from $K^\pm \to \pi^0\pi^\pm$, and from the Mainz A2 collaboration [22], an analysis of approximately 0.5 M reconstructed Dalitz decays from $\gamma p \to \pi^0 X$ at the $\Delta(1232)$. The A2 collaboration plans to continue data taking and expects to obtain an additional 2 M reconstructed events. NA62 and A2 obtained $a_\pi = .0368(51)_{stat}(25)_{sys}$, and $a_\pi = .030(10)_{total}$ from the analysis of their data, respectively. A compilation of time-like slope parameter measurements is shown in Fig. 6, where the parameter $\Lambda^2 = m^2_\pi/a_\pi$ is plotted in the figure.

The PDG gives $a_\pi = .0335 \pm .0031$ for the slope parameter, an error of $\pm 9\%$. The PDG average is dominated by two results; (i) NA62 and (ii) the result from fitting the CELLO

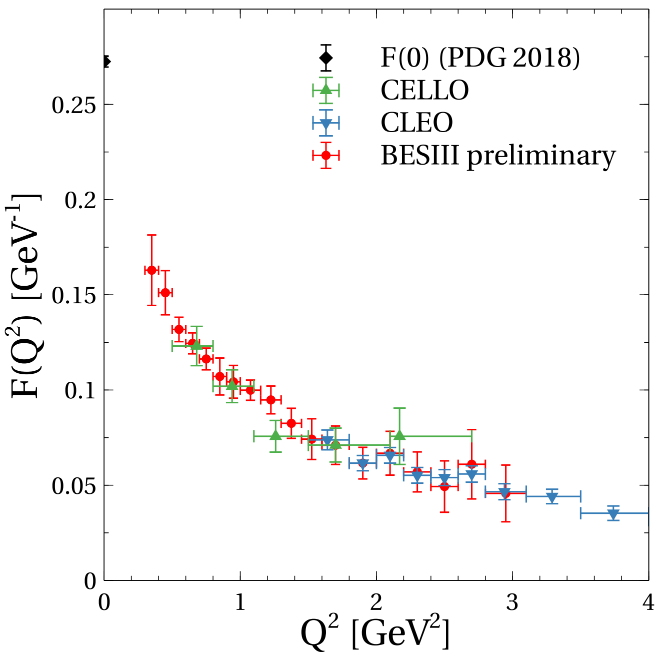

Figure 5: Momentum dependence of the space-like π^0 TFF for $Q^2 \leq 4\ GeV^2$. Data from CELLO[18] (green triangels (up)), CLEO[19] (blue triangles (down)), and preliminary data from BESIII[20] (red circles). Fig. taken from Ref. [3]

data points with a VMD form factor[18]. The slope parameter in the CELLO analysis is obtained from an extrapolation of the data at $0.6 \leq Q^2 \leq 2.2$ to $Q^2 \to 0$. The estimated combined statistical and systematic error on the extrapolation is $\pm 11\%$ for a_π.

Finally, we note that there is a significant data set on the *time-like* π^0 TFF measured in the reaction $e^+e^- \to \gamma^* \to \pi^0\gamma \to 3\gamma$ from CMD-2[23] and SND [24, 25, 26]. However, there isn't a simple method to translate the TFF measured in the time-like region into the space-like region. Analytic continuation methods such as dispersion calculations must be utilized, hopefully without introducing a significant model dependence [3, 4].

In summary, based on the disagreement of a_μ^{exp} with a_μ^{SM}, FNAL E989 may soon reach the 5σ "gold standard" for the discovery of physics beyond the Standard Model. Given the importance of this possible discovery, we believe that existing experimental constraints on the low-Q^2 region of the π^0 TFF are inadequate for a precision measurement of $a_\mu^{HLbL-\pi^0}$, which is the largest component of HLbL.

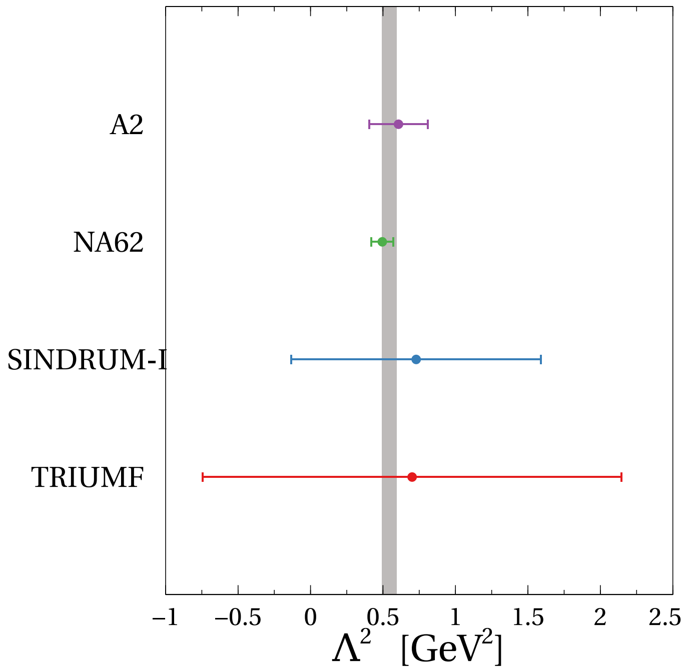

Figure 6: Slope parameter $\Lambda^2 = m_\pi^2/a_\pi$ of the timelike π TFF from Dalitz decays. The gray band shows the current average value and its uncertainty listed by the PDG. Fig. taken from Ref. [3]

4 Experimental Setup

The proposed TFF measurement will use the PRad setup shown in Fig. 7, but with several critical improvements and changes that include (i) a flash-ADC based readout system for the calorimeter, (ii) an additional GEM detector plane, and (iii) a solid target. The scattered electrons and π^0 decay photons will be detected simultaneously in HyCal, the calorimeter successfully used in the PrimEx-I, PrimEx-II, and PRad measurements

4.1 Beamline and detectors

Just as in the PRad experiment, the scattered electrons will travel through the 5 m long vacuum chamber with a thin windows to minimize multiple scattering and backgrounds. The vacuum chamber matches the geometrical acceptance of the calorimeter. The new GEM plane will be placed about 40 cm upstream of the GEM plane used in PRad, as shown in Fig. 8. The pair of GEM planes will ensure a high precision measurement of the GEM detector efficiency, and add a modest tracking capability to further reduce the beam-line background.

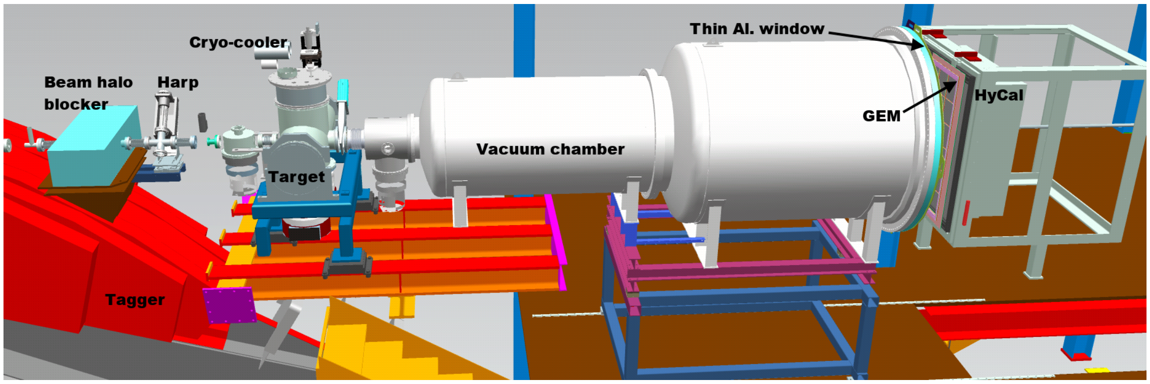

Figure 7: A schematic layout of the PRad experimental setup in Hall B at Jefferson Lab, with the electron beam incident from the left. The key beam line elements are shown along with the two-segment vacuum chamber, and the GEM and HYCAL detector systems.

The principle elements of the experimental apparatus along the beamline are as follows:

- Two stage, large area vacuum chamber with a single thin Al. window at the calorimeter end
- Silicon target of thickness $250\mu m$
- A pair of GEM detector planes separated by about 40 cm for coordinate measurement as well as tracking.
- HyCal calorimeter with high resolution $PbWO_4$ crystal calorimeter insert in the interior, and lead glass blocks on the exterior. The HyCal readout electronics should be converted from the FASTBUS(!!!!!!) based system used for PrimEx-I, PrimEx-II and PRad, to the standard JLab flash-ADC based system.

The PRad collaboration has proposed upgrading the HyCal calorimeter to be an all $PbWO_4$ calorimeter, rather than the hybrid version. In this upgrade the lead-glass modules would be replaced with new $PbWO_4$ crystals, significantly improving the uniformity of the electron detection over the entire experimental acceptance. While this upgrade is welcomed for the proposed TFF measurement, it is not essential. All of the simulations in this proposal assume the standard (non-upgraded) HyCal.

We note that the precision of the GEM detector efficiency contributed significantly to the systematic uncertainty of the PRad experiment. A high precision measurement of the GEM detector efficiency can be achieved by adding a second GEM detector plane. In this case, each GEM plane can be calibrated with respect to the other GEM plane instead of relying on the HyCal, minimizing the influence of the HyCal position resolution.

It will also help reduce various backgrounds in the determination of the GEM efficiency, such as cosmic backgrounds and the high-energy photon background. In addition, the tracking capability afforded by the pair of separated GEM planes will allow measurements of the interaction point coordinate along beamline. This can be used to eliminate various beam-line backgrounds, such as those generated from the upstream beam halo blocker. The uncertainty due to the subtraction of the beam-line background, at forward angles, is one of the dominant uncertainties of PRad. Therefore, the addition of the second GEM detector plane will reduce the systematic uncertainty contributed by two dominant sources of uncertainties. Collaborators at UVa have committed to the construction of the second GEM plane.

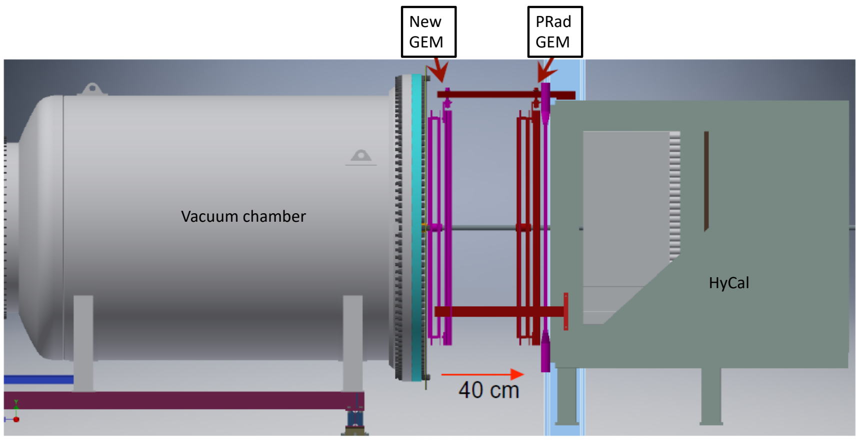

Figure 8: The placement of the new GEM chamber in the proposed experimental setup for PRad-II.

Important upgrades are planned **(in progress?, completed?)** for the Hall-B beamline. The window on the Hall-B tagger is being **(has been?)** replaced with an aluminum windows which is expected to result in a significant improvement in the beamline vacuum, particularly upstream of the target. This will help reduce one of the key sources of background observed during the PRad experiment. Further, a new beam halo blocker will be placed upstream of the Hall-B tagger magnet. This will further reduce the beam-line background critical for access to the lowest angular range and hence the lowest Q^2 range in the experiment.

4.2 Silicon target

Primakoff experiments typically use targets with moderate atomic number (for a reasonable ratio of Primakoff to coherent production), ground state $J^\pi = 0^+$ (to simplify the reaction mechanism), precisely determined nuclear charge distribution (for calculation of E.M. and strong form factors), and targets that are not difficult to handle (for thickness studies and mounting). Silicon satisfies all of these criteria. Because of the success PrimEx-II had with data taking on silicon (see fig. 2), and the considerable effort that went into calculation of the coherent and incoherent backgrounds for silicon, we elected to utilize silicon as the target in the TFF measurement.

The target will be an approximately $250\,\mu m$ thick silicon crystal disk, diameter from 1 to 2 inches, with natural isotopic abundance. This thickness is approximately $0.3\,\%$ radiation length. The amount of n-doping or p-doping in these silicon crystals is effectively negligible for our purposes. To better understand multiple scattering effects in the data we will also take calibration data with a $100\,\mu m$ thick silicon target mounted on the target ladder. Si wafers of this size and thickness are available from several manufacturers.

Electrons passing through crystal radiators produce coherent radiation (peaked at specific energies) and non-coherent radiation (with characteristic $1/k$ distribution), and also experience channeling affects. For this experiment it's preferable for the Si crystal to behave similar to a non-crystalline target. The simplest way to do this is to not align the principle symmetry axis of the Si crystal, the (1,0,0) crystal orientation, with the beam-line. We will consider using a Si wafer with (1,1,1) orientation, or a Si wafer with (1,0,0) orientation and rotate the normal vector to the disk around the beam-line x and y axes by $\approx 45\,^{\circ}$.

Silviu Dusa at JLab has performed an assessment of target beam heating using the computational fluid dynamics (CFD) code ANSYS-FLUENT. Fig. 9 shows the calculated equilibrium target temperature across the central axis of the target assuming a 25 mm diameter, $25\,\mu m$ thick Si target, and an unrastered $0.55\,\mu\,\mathrm{A}$, $100\,\mu m$ diameter electron beam. The figure indicates a modest central temperature rise of $\approx 2^{\circ}\,\mathrm{K}$. For the proposed running conditions of TFF, $250\,\mu m$ thick Si and 10 nA beam, beam heating is reduced by a factor of ≈ 0.2 relative to the CFD calculation shown here. Therefore, we conclude that target beam heating is not a limiting factor in setting the luminosity of the measurement.

4.3 DAQ trigger

The TFF experiment requires that the original HyCal FASTBUS readout electronics be replaced with borrowed or new JLab flash-ADC modules. A total of 1,728 channels of fADC are required to instrument the 1,152 channels of $PbWO_4$ crystal, and 576 channels of lead-glass blocks. We are in discussions with the Hall B DAQ group as to the best path forward to realize this requirement.

The DAQ trigger for the proposed TFF experiment will be organized from flash-ADC energy measurements in each block of HyCal. The trigger schemes under study require two or three clusters of energy in HyCal, each with energy greater than 0.3 or 0.4 GeV, and with a total energy sum of 4 GeV or greater. This type of trigger will be able to effectively select the expected three electromagnetic particles in the final stage of the reaction (the scattered electron and two decay photons from the forward produced neutral

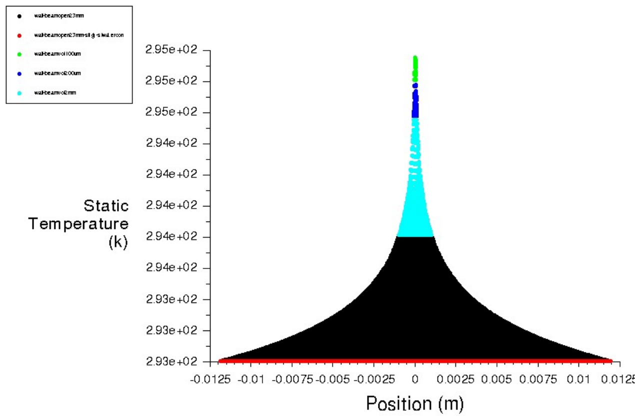

Figure 9: Beam heating of a 25 mm diameter, 25 μm thick Si target for a 0.55 μA, 100 μm diameter, unrastered electron beam.

pion). The only significant contamination will be from time-accidental events from either deep inelastic scattering eA, and/or e^-e^--Moller production, both of which are high cross section processes. However, the good timing resolution of HyCal equipped with the FADC electronics (~ 2 ns) will make these out-of-time backgrounds a small part of the total DAQ trigger rate.

Estimated trigger rates are presented in section 6.

5 Acceptances and resolutions

The proposed experimental setup is sensitive to elecron scattering angles θ_e larger than $\sim 0.6°$. In this section we present our results for the Primakoff cross section (see Eqn. 2) calculated using the technique described in Ref. [27]), and with acceptance related to the $\theta_e > 0.5°$ limitation.

Figure 10 shows the Primakoff differential cross section as a function of the scattered electron energy for Q^2 ranges 0-0.3 GeV^2 and 0-1.0 GeV^2, and constant π^0 transition form factor ($F_{\gamma^*\gamma^*\to\pi^0} \equiv 1$). The corresponding integrated cross section values are 2.31 nb and 2.36 nb.

Geometric acceptance and reconstruction efficiency for Primakoff production have been estimated with the GEANT Monte-Carlo package. Simulated events were reconstructed using a program similar to that used for the HyCal calorimeter in the PrimEx-II experiment. The selection criteria for reconstructed events to be accepted were: (i) minimum energy

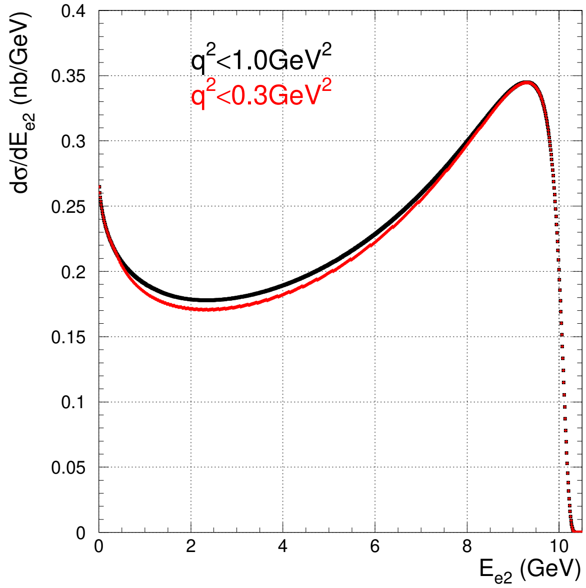

Figure 10: Primakoff differential cross section integrated over solid angles as a function of the scattered electron energy for Q^2 in the range 0-0.3 GeV^2 (red dots), and 0-1.0 GeV^2 (black dots) ranges. In this plot the incident electron energy is $E_0 = 10.5$ GeV, and the π^0 TFF is taken to be constant, $F_{\gamma^*\gamma^*\to\pi^0} \equiv 1$

of 0.5 GeV for a particle in the calorimeter (this is the same threshold PrimEx-II used for HyCal reconstruction); (ii) maximum energy of 4.5 GeV for the scattered electron, as acceptance drops sharply at this energy (see Fig. 11); (iii) the reconstructed π^0s should have an invariant mass within $\pm$ 10 MeV of 135 MeV (this is approximately 3 detector resolution **neither FWHM's or σ's. it is actually weighted mean of two σs from double gaussian fit shown on the fig.**); (iv) energy conservation in the detected event within $\pm$ 0.5 GeV; (v) γ's from π^0 decay should not overlap with charged particles in the GEM detector within 2 cm in both the X- and Y-directions. The charged particles can originate from the same event, or be accidental beam electrons within the 40 ns time acceptance window. Obtained efficiencies as a function of Mandelstam t and Q^2 for the Primakoff π^0 electro-production are shown in Figs. 12 and 13. The plots show that the efficiency is very significant, 30% or higher, for the main region of interest, $0.01\,GeV^2 < Q^2 < 0.3\,GeV^2$.

The π^0 invariant mass resolution $\sigma \sim 3.3$ MeV, and total event energy resolution $\sigma \sim 150$ MeV are shown in Figs. 14, and 15. The mass resolution is worse than the 2.4 MeV value obtained in the PrimEx-II analysis because we are using the entire hybrid calorimeter, including the lead glass part, whereas PrimEx-II used just the lead-tungstate crystal insert. The relative Q^2 resolution as a function of Q^2, $\sim 3\,\%$, is shown in Fig. 16. Man-

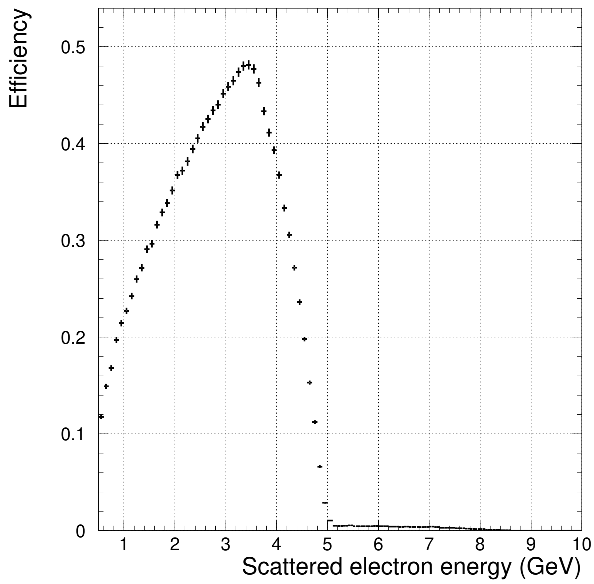

Figure 11: Detection efficiency vs scattered electron energy at an incident electron energy of $E_0 = 10.5$ GeV

delstam t resolution divided by $\sqrt{t}$ is shown in Fig. 17. Figs. 18 and 19 show the resolution in θ_π, the angle between the virtual photon beam momentum $\vec{q}$ direction and the neutral pion momentum $\vec{k}_\pi$ direction. This resolution is in the 0.02°-0.03° range, close to the resolution obtained in PrimEx-II. Resolutions of this order are more than adequate to resolve the Primakoff peak from the coherent background (see Fig. 2). The electron scattering angle resolution will depend on the target thickness. Fig. 20 shows the scattering angle resolution for a 250 μm thick silicon target as a function of the scattered electron energy. The resolution roughly follows a $\frac{0.024^\circ}{(E_e[GeV])^{0.85}}$ dependence, shown by the dashed line in the figure.

Fig. 21 shows the Primakoff differential cross section integrated over scattered electron solid angle and energy (within 0.5–4.5 GeV range) as a function of the π^0 production angle. The corresponding simulated π^0 yield scaled to the proposed 60 days of running is shown in Fig. 22. The Primakoff maximum is shifted from 0.02° to 0.04° due to resolution.

We conclude that the proposed experiment entirely complements the BESIII and CELLO measurements in covering the low Q^2 region with good acceptance and resolution.

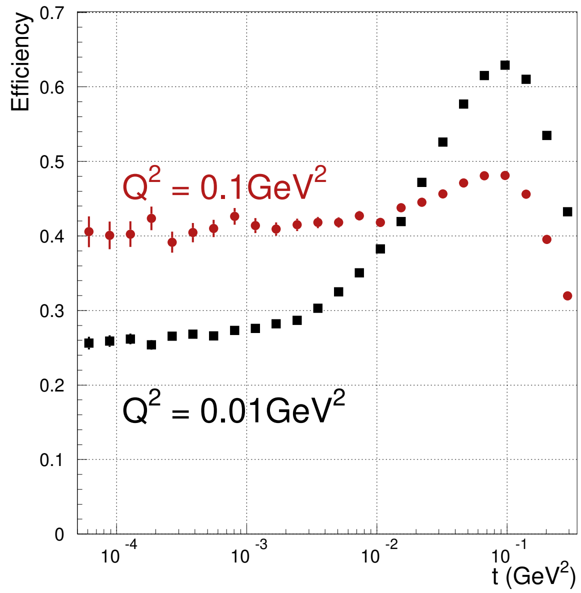

Figure 12: Detection efficiency vs Mandelstam t for $E_0 = 10.5$ GeV, scattered electron energy range 0.5...4.5 GeV, and $Q^2 = 0.01\,\mathrm{GeV}^2/c^2$ (black squares), and $Q^2 = 0.1\,\mathrm{GeV}^2/c^2$ (red dots).

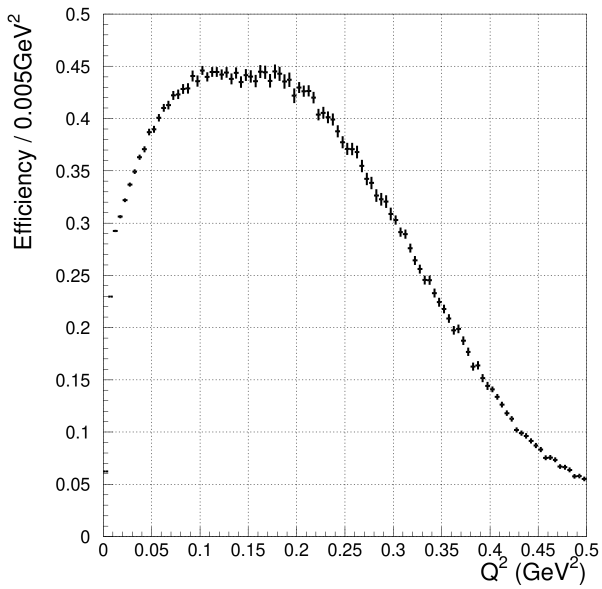

Figure 13: Detection efficiency integrated over Mandelstam t vs Q^2 for $\mathrm{E}_0 = 10.5\,\mathrm{GeV}$, and scattered electron energy range 0.5...4.5 GeV

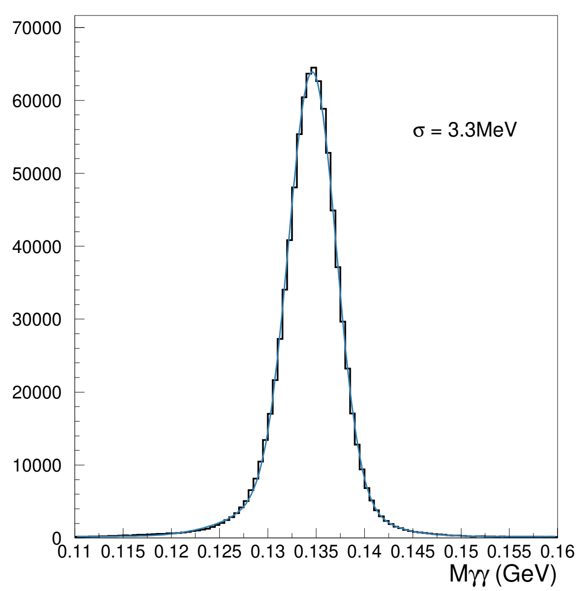

Figure 14: π^0 invariant mass resolution

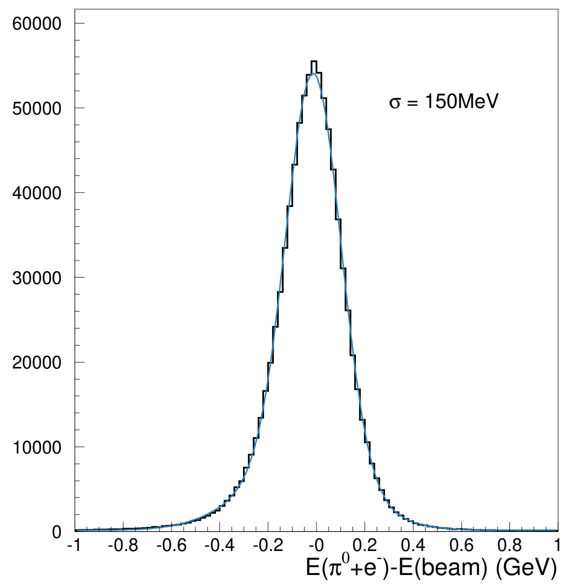

Figure 15: Event total energy resolution

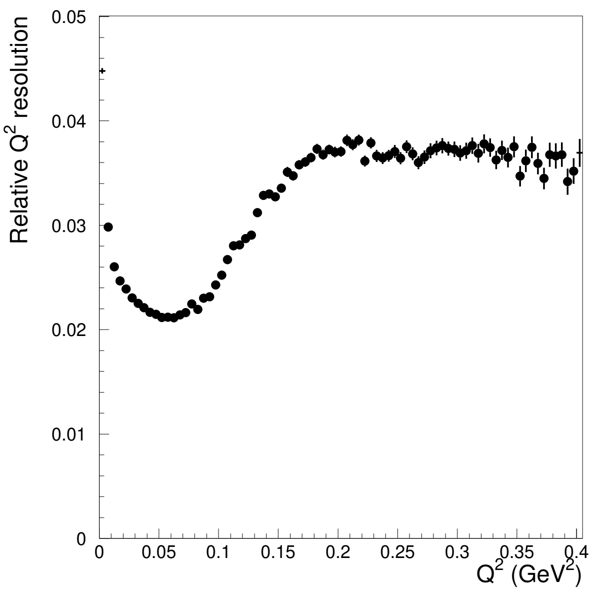

Figure 16: Relative Q^2 resolution vs Q^2, $E_0 = 10.5\,\mathrm{GeV}$

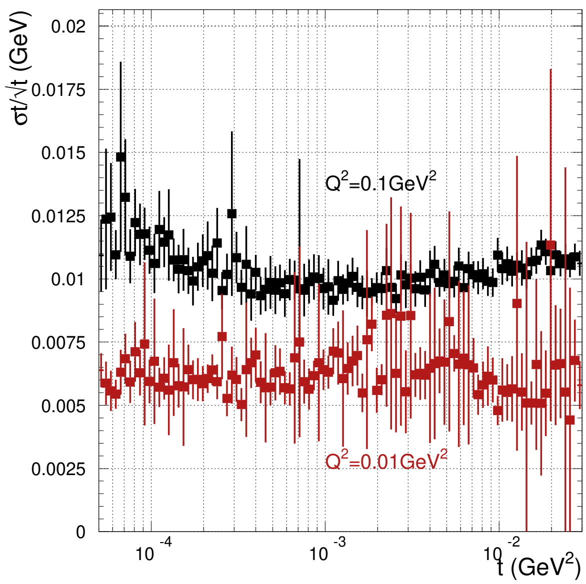

Figure 17: t resolution over $\sqrt{t}$ as a function of t for $\mathrm{Q}^2 = 0.01$ (red points), and $0.1\,\mathrm{GeV}^2$ (black points), $\mathrm{E}_0 = 10.5\,\mathrm{GeV}$

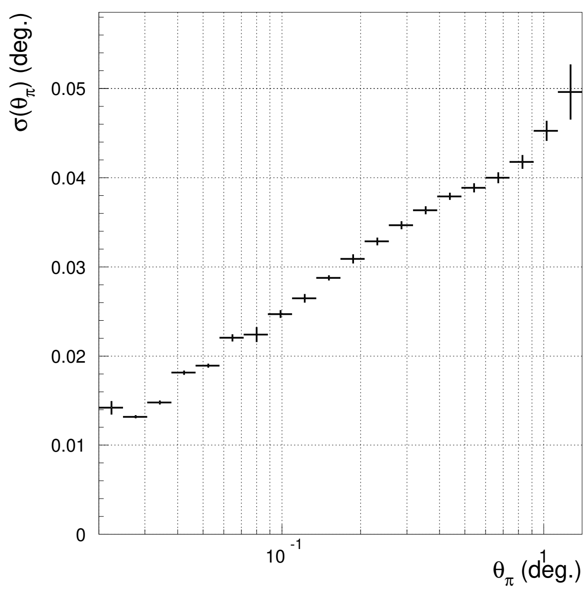

Figure 18: Resolution in θ_π vs θ_π, at E_0 = 10.5 GeV. θ_π is the angle between the virtual photon beam momentum $\vec{q}$ and the neutral pion momentum $\vec{k}_\pi$.

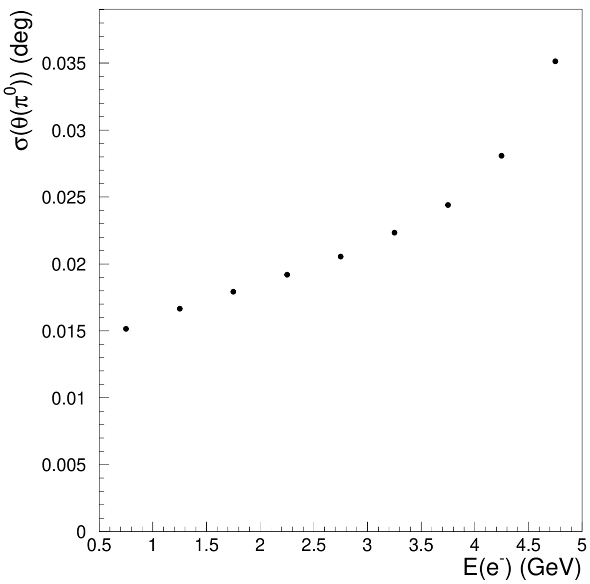

Figure 19: Resolution in θ_π vs scattered electron energy, at $E_0 = 10.5$ GeV

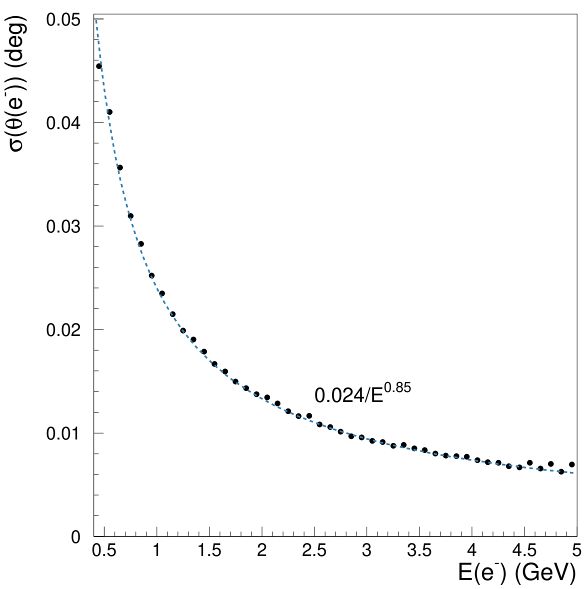

Figure 20: Resolution in the electron scattering angle vs scattered electron energy, at $E_0 = 10.5$ GeV. The dashed line shows the $\frac{0.024^\circ}{(E_e[GeV])^{0.85}}$ fit.

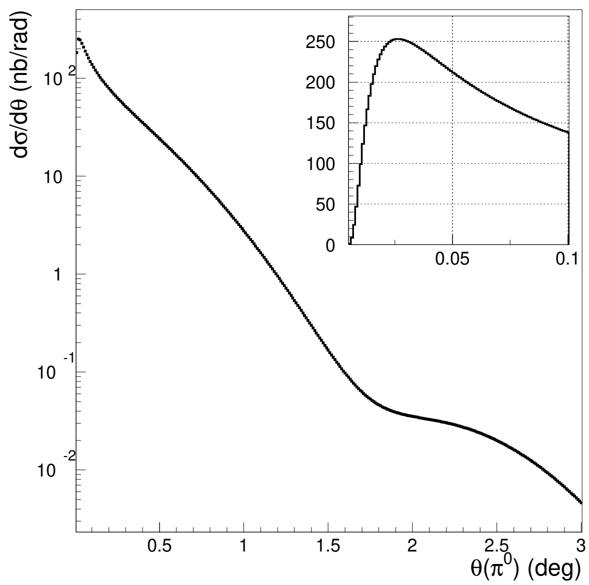

Figure 21: Primakoff differential cross section integrated over scattered electron solid angle and energy (within 0.5–4.5 GeV range) as a function of π^0 production angle

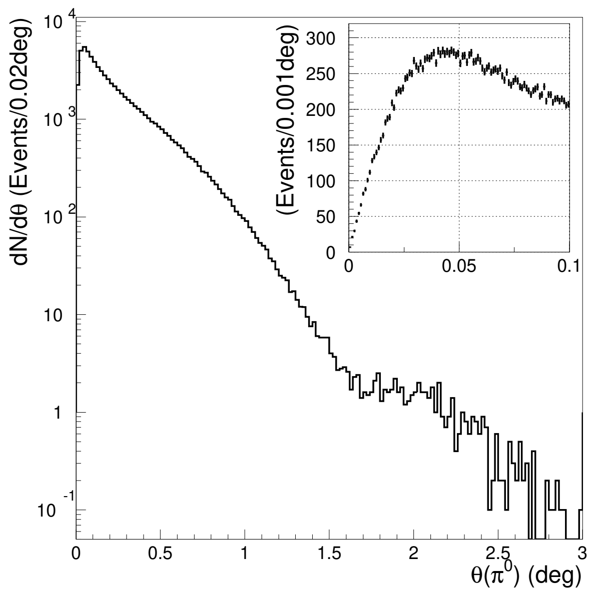

Figure 22: Simulated π^0 yield scaled to the proposed 60 days of running statistics as a function of π^0 production angle

6 Trigger rates and radiation dose

To estimate trigger rate and radiation dose in the calorimeter we have performed simulations of electromagnetic processes in the target and their effect on HyCal response caused by the electron beam using GEANT program package.

The main contributions to the background rate are from (i) delta electron production, and (ii) multiple scattering in the target, the latter causing the incident beam to interact sometimes with the inner layer of the calorimeter. Bremsstrahlung production also contributes to the background, with a rate smaller than the other two backgrounds. Rates have been estimated based on the luminosity proposed to PAC 48 in our letter of intent: $25\,\mu$m silicon target and 100 nA electron beam current. Since the multiple scattering affect grows slower than linear with increasing target thickness, we tested several combinations of target thickness and beam current while keeping the product of the two constant to see how best to optimize the experiment. The main limiting factor for the product is the channel rate in the inner-most part of HyCal, caused primarily by the scattered incident electron beam. To keep this contribution at an acceptable level, we plan to increase the thickness of the tungsten absorber installed in front of the central HyCal crystals from 6 to 15 cm, and expand the transverse size of the absorber from 4×4 to 6×6 HyCal modules. Fig. 23 shows calorimeter module rates for the most background loaded layers as a function of target thickness and beam current, with the product being held fixed. Even with the increased absorber thickness the rate in the most inner layer of HyCal is still too high – more than 2 MHz for the thinnest target, and caused primarily by the scattered incident beam hitting the central crystals. Therefore, we propose to turn off HV for this layer. The rate in the second inner layer protected by the enlarged absorber is acceptable, within 250 kHz.

Fig. 24 shows the radiation dose rate for layers in HyCal. For the inner-most layer the radiation dose is from 8 to 10 rad/hr if not considering the $50\mu m$ target, and 4 to 6 rad/hr for the next four outer layers. According to studies [28, 29] this may result in a 2%–5% light yield degradation in the module due to the radiation effects.

Fig. 25 shows the calorimeter trigger rate for a simple 4 GeV total energy threshold. The trigger rate is estimated to be approximately 250 kHz, which is unworkable for the experiment. For that reason we require the implementation of the more sophisticated trigger scheme described in section 4.3.

Fig. 26 shows the estimated trigger rate when two or three clusters are required in the calorimeter, each cluster with energy greater than 0.3 or 0.4 GeV, and a total energy sum of 4 GeV or greater. Clusters are defined as simple 3×3 module areas in HyCal which may not intersect with each other. In this case the trigger rate reduces to 25 kHz at the highest and 4 kHz at the lowest, which can be handled by the Hall-B DAQ system.

Using HyCal energy deposition in the trigger requires the gain equalization procedure to avoid systematics related to the trigger inefficiency. This will be done by placing HyCal on the transporter and scanning in the low intensity photon beam produced in the photon tagger with the electron beam energy reduced to about 5 GeV. This procedure has been performed previously during the PrimEx and PRad experiments and takes about 3 days of beam time and 3 days for placing HyCal on the transporter and back.

In summary, we propose to switch off HV for the inner-most layer in HyCal, increase the tungsten absorber transverse size by factor of 1.5, and thickness by 2.5. The trigger should be configured to require two or three clusters of energy in the calorimeter, each with energy greater than 0.3 or 0.4 GeV, and with a total energy sum requirement of 4 GeV. Running with a 250 μm Si target and 10 nA beam current gives an estimated trigger rate in the 3.5 to 20 kHz range. The estimated DAQ trigger rates and radiation dose to the HyCal modules are estimated to be acceptable for running the experiment.

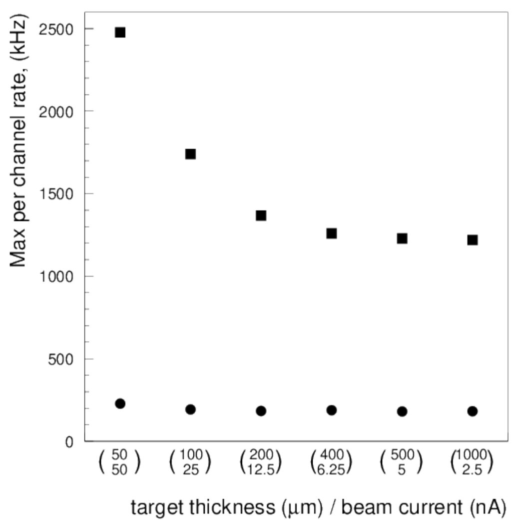

Figure 23: Estimated HyCal module rates. Squares – most inner HyCal layer around the beamline, circles – the seond inner layer.

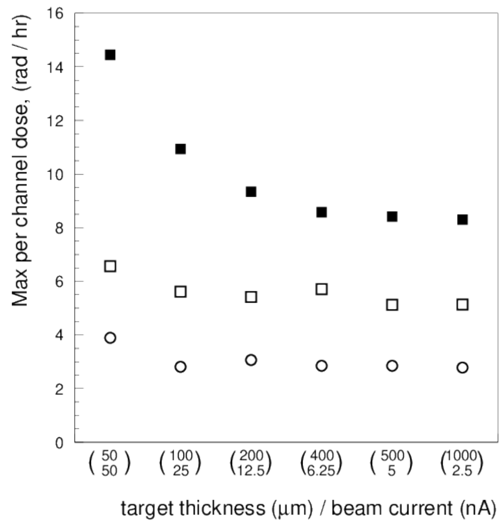

Figure 24: Estimated radiation dose rate per hour. Solid squares – most inner HyCal layer around the beamline, open squares – the third inner layer (first unshielded layer), open circles – area outside the third inner layer.

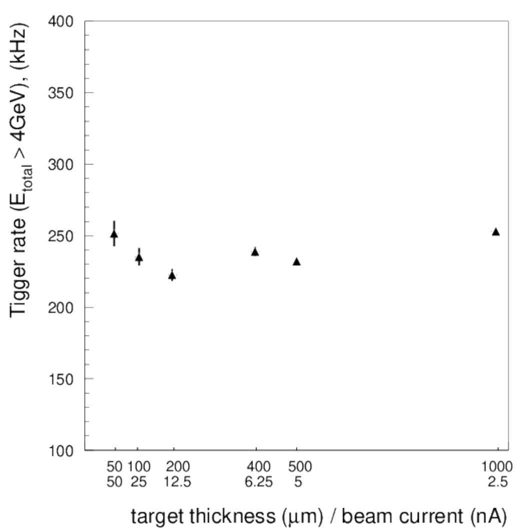

Figure 25: Estimated HyCal trigger rates for the simple total energy sum trigger with the threshold of 4 GeV

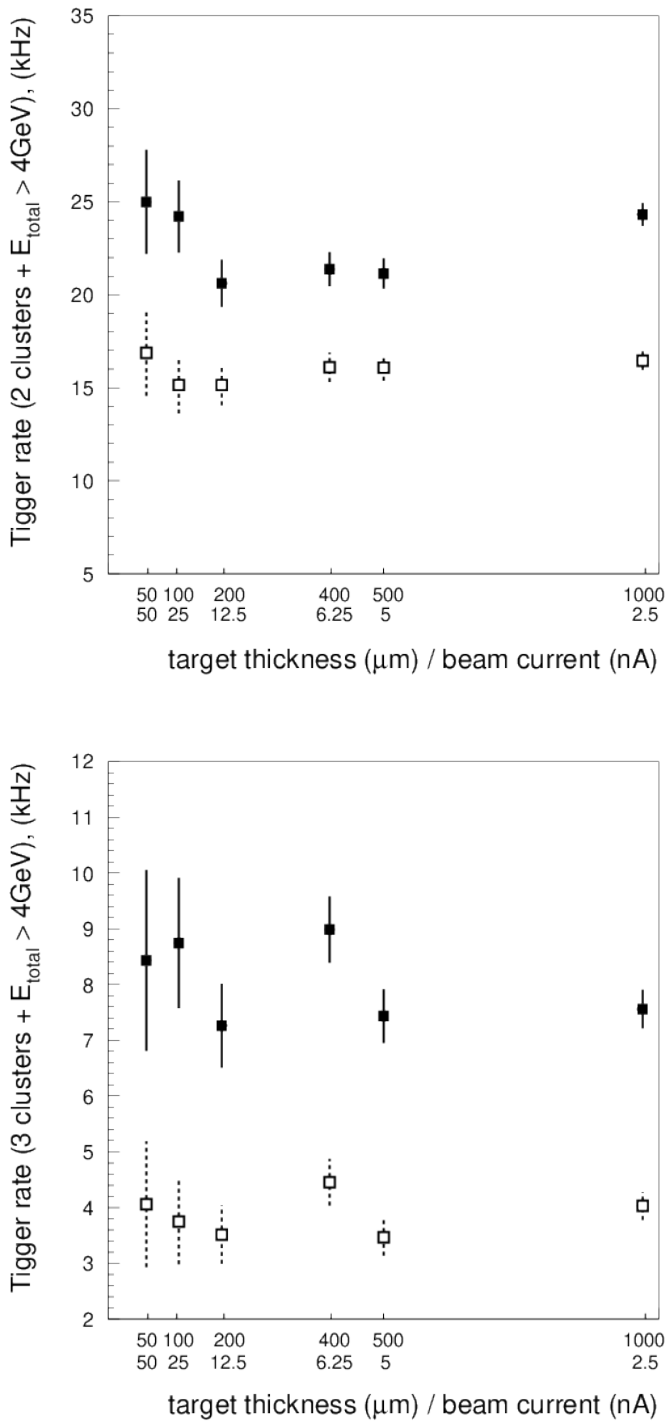

Figure 26: Estimated trigger rates for events with total energy deposition in HyCal more than 4 GeV and at least two clusters (top), or three clusters (bottom) found. The minimum cluster energy is 0.3 GeV (solid squares), or 0.4 GeV (open squares).

7 Data Rates

7.1 Signal yield

To estimate the integral event rate for the Primakoff events we ran MC simulations with the following fixed parameters and intervals:

- Target: 250 μm silicon
- Beam energy: 10.5 GeV
- Beam current: 10 nA
- Angular range of the scattered electrons: $> 0.5^\circ$
- Energy range of the scattered electrons: $0.5 \div 4.5$ GeV
- Full range of expected Q^2 values up to 1 GeV^2
- γs from neutral pion decays should have energy at least 0.5 GeV, and not overlapped with any charged particle in the GEM detectors

The total Primakoff cross section integrated over the scattered electron energy range of 0.5...4.5 GeV is estimated to be $\Delta\sigma = 0.65 \cdot 10^{-3}\,\mu b$. With these numbers and simulated geometrical acceptance, the Primakoff event rate in the proposed experiment is ≈ 1150 events/day or $\approx 69{,}000$ events/60 days. Therefore, for an estimated 60 days of beam time we will be able to accumulate approximately 60,000 useful events over the Q^2 range from .003 to 0.3 GeV^2.

7.2 Background levels

There are two main contributions to the background: electromagnetic and hadronic.

To estimate the backgrounds from electromagnetic processes extensive studies have been performed: 6×10^{15} events of the electron beam interacting with the 250 μm thick silicon target have been simulated. This corresponds to about 26.5 hours of 10 nA beam current. Events were sampled by 40 ns bunches with 2,500 events per bunch. Bunches with at least 7.5 GeV total energy deposition in the calorimeter and 3 particles each with a minimum energy of 50 MeV going into the calorimeter acceptance (including the absorber area) have been recorded for further processing. The selected events have been propagated through the experimental setup and reconstructed. During reconstruction we assumed that charged particles (mostly electrons) can be misidentified as neutrals with 1% probability, which is a reasonable estimation based on our previous experience with the PRad GEM. In the reconstructed event we selected particles with energy greater than 0.5 GeV, and required that there should be at least two neutral particles for π^0 reconstruction and a third one

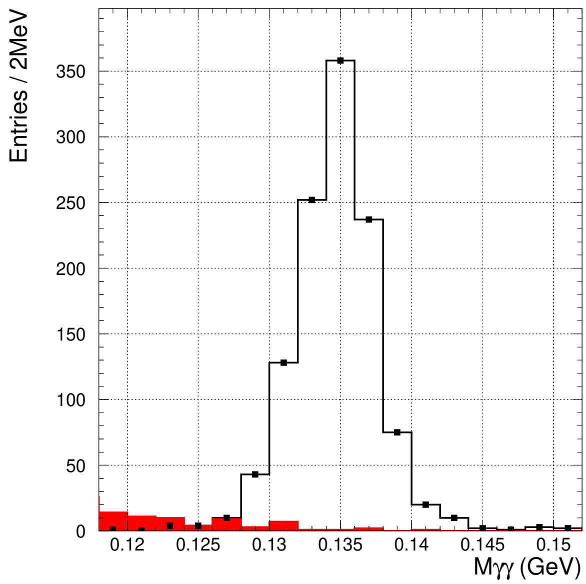

Figure 27: Invariant mass of two neutral clusters in the calorimeter. Expected statistics for one day of running. Open histogram – Primakoff π^0, red solid histogram – electromagnetic background

(mimicking the scattered electron) with the total energy of triplet within a ± 1 GeV window around the beam energy. The result of this background simulation for the invariant mass of the false π^0 candidates is shown in Fig. 27. We put the expected events from Primakoff production for the same running time, one day of running, on the same plot for comparison. We note that the calorimeter timing resolution obtained during the PrimEx experiment was better than 2 ns, which should suppress most of the background obtained with the ± 20 ns timing window shown in Fig. 27. The dependence of the number of background events as a function of the coincidence time window is shown in Fig. 28.

The main hadronic backgrounds are from π^0 and ω meson photo-production on the target (with "forward" $\omega \to \pi^0\gamma$ decay), with the incident real photon produced by bremsstrahlung in the target. To pass the analysis selection criteria these processes must have a complementary electron that satisfies the energy conservation condition. The electron in the event could be either an incident beam electron rescattered in the target, or any background electron that's accidentally in time and satisfies energy conservation with the π^0, i.e. within $3\,\sigma$ of the apparatus energy resolution. The virtual photon beam angle in the lab frame has values in the range from 0 up to $\sim 1^\circ$. The direct π^0 photoproduction cross section is well studied [1] and has cross section of $\sim 1.5\,\mu b$ (at 5 GeV photon beam energy) if integrated from 0 to 2.4° angle of the pion. With the proposed experimental setup we estimate the

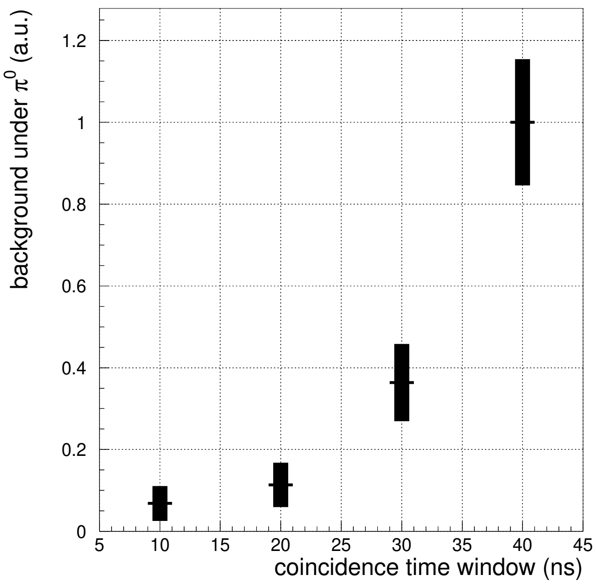

Figure 28: Dependence of the number of electromagnetic background events underneath π^0 mass peak as a function of the coincidence time window size

background yield contribution from this process to our data within 50 events for the entire run. ω meson photoproduction cross sections have values of $\sim 30\,\mu b$ (coherent mechanism), and $\sim 70\,\mu b$ for the incoherent contribution, [30, 31]. Even this source has a significantly higher cross section, it is suppressed by $\omega \to \pi^0\gamma$ decay branching and, in addition, the scattered electron can not satisfy the energy conservation (only accidental scattered beam electrons can be coupled with such pions to pass through analysis criteria). Our estimation for this background yield contribution is below 350 events for the 60 days of running. Thus we expect the total hadronic background contribution to be within a percent level and to affect the measurement systematics well below percent level.

8 Cross section normalization

In addition to the direct electron beam flux measurement, which we expect to have an uncertainty at sub-percent level, we will use Moller scattering for the additional normalization. This process is well studied and can easily be measured with very high statistics. It has a very distinct signature: relationship between scattered electron energy and angle. The setup provides the excellent acceptance for such measurement by detecting one of two scattered electrons. Fig. 29 shows two dimensional distribution of scattering angle and energy for the outgoing electrons. We will setup an additional total energy deposition in

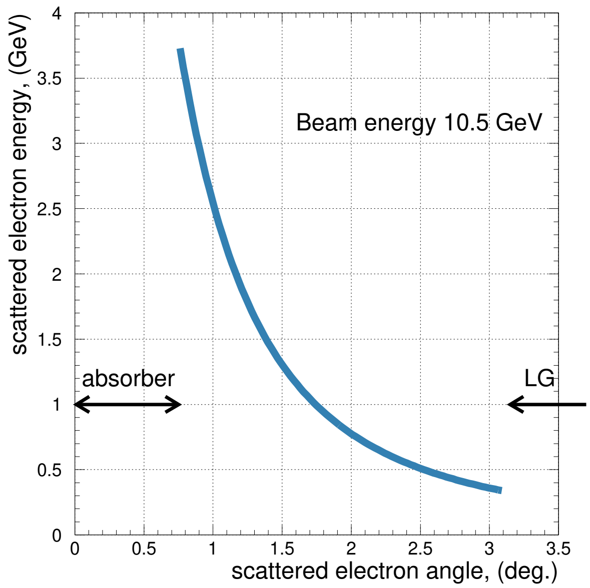

Figure 29: 2-dimensional distribution of Moller scattering electrons energy and angle. Arrows show regions corresponding to absorber and lead glass part of the calorimeter.

the calorimeter trigger to record such events with the threshold of $\sim$1 GeV for the inner part (12x12 modules) and $\sim$ 0.2 GeV for the outer part, which will be scaled by 3 orders of magnitude. The exact energy thresholds and scale factors will be briefly optimized during commissioning run after the gain equalization procedure. Such a measurement will have the most of the contributions to the systematic uncertainty the same as we observed during the neutral pion photoproduction cross section measurement [1], which have value of 0.7...0.8%. In conjunction with the direct beam flux measurement we expect to have the luminosity uncertainty control at the sub percent level.

9 Results from fitting pseudo-data: projected sensitivities

To estimate this experiment sensitivity to the TFF parameters [equation 1], we have simulated data samples with Coulomb [eq. 2], strong coherent [eq. 11] production mechanisms and their interference. We have taken for the simulations the interference phase value of 1 rad observed in photoproduction on silicon [1]. The expected yield for the proposed luminosity shown in fig. 30, production mechanisms contributions shown in color curves. To extract TFF parameters, the simulated data were split in 30 bins of Q^2: from 0 to 0.3 GeV^2, then the Coulomb yield was normalized to the expected yield from the simulation with TFF set to 1.

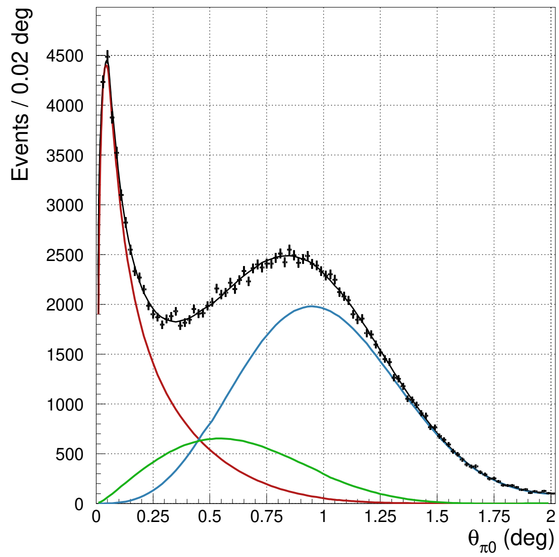

Figure 30: Simulated detected yield for π^0 electroproduction. Curves show input from Coulomb (red), strong coherent (blue), and their interference (green) production mechanisms.

In our analysis we fit the distribution for square root of the resulting ratio (fig.31) with the simple equation: $\sqrt{Yield\ ratio} = Constant - Slope \cdot Q^2 + Quadrature\ term \cdot Q^4$. For the expected statistics we are able to extract slope and quadrature parameters (correspond to a_π and b_π in eq. 1) with the relative uncertainties of 6 % and 17 %, and constant term with uncertainty of 0.35%, which corresponds to 0.7% stat. error in $\pi^0 \to \gamma\gamma$ decay width.

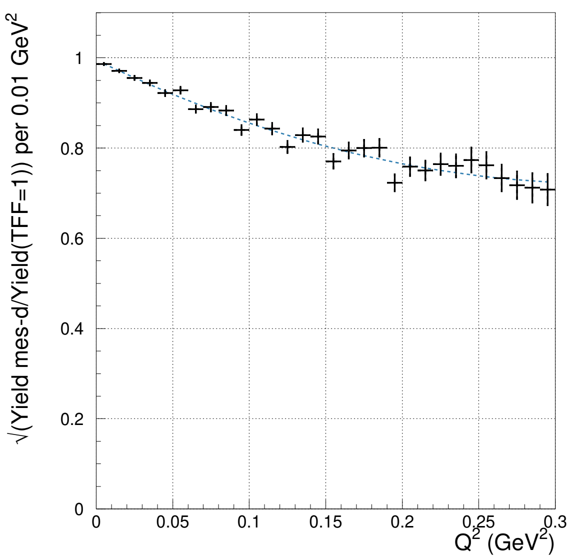

Figure 31: Square root of the realistic yield and yield simulated with the constant TFF=1 ratio split in Q^2 bins. Curve shows fit result.

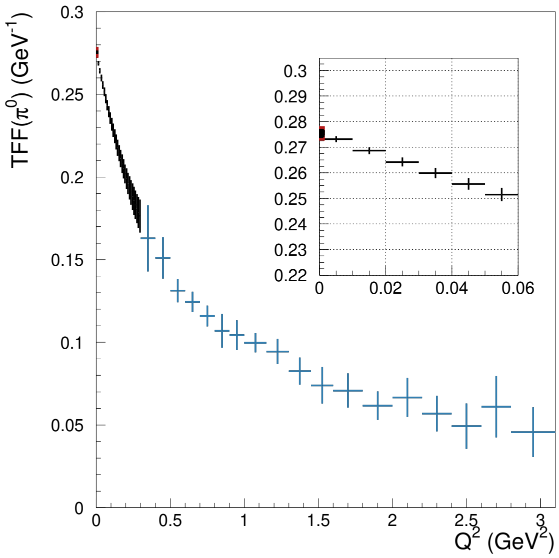

Figure 32: Momentum dependence of the π^0 TFF. Preliminary data from BESIII[20] (blue histogram), PrimEx measurement (red point at $Q^2 = 0$), and the projected proposed measurement (black histogram).

10 Summary of the proposed experiment and impact on studies of fundamental symmetries

This needs to be reworked, it mostly came from the LOI, need many more details here and deliverables

The measurement of the π^0 TFF through the Primakoff reaction with virtual incident photons would run using the PRad-II setup in Hall B. Both the scattered electron and the two decay photons will be detected in HYCAL, with GEMs used for electron tracking. The proposed measurement has sensitivity to the TFF over a Q^2 range from .003 - 0.3 GeV^2, allowing a clean determination of the slope and curvature parameters in the TFF, and complementing the spacelike BESIII and CELLO measurements at Q^2 $>$ 0.3 GeV^2, and Dalitz decay measurements in the timelike region. The cross sections are proportional $\Gamma_{\pi^0 \to \gamma\gamma}$, the neutral pion decay width, and we will also pursue this as an experimental goal if feasible. We note that hadronic light-by-light scattering, one of the largest uncertainties in the Standard Model prediction for muon $g-2$, critically depends on knowledge of the pseudo-scalar meson TFFs in the low Q^2 region.

A Nuclear coherent scattering

This is where we describe Sergey's work on nuclear coherent scattering.

$$\frac{d^3\sigma_S}{dE_2 d\Omega_2 d\Omega_\pi} \quad = \quad \left| \frac{A g_{\omega\pi\gamma}\, g_{\omega NN}\, R_\omega}{4\pi m_\pi} \right|^2 \frac{\sigma_M}{\pi} \frac{\beta_\pi^{-1}}{E_\pi} \left| F_N(t) \right|^2 sin^2(\frac{\theta_e}{2}) sin^2(\theta_\pi) k_\pi^4 E_1 E_2 \quad (11)$$

where A - number of nucleons in nucleus; $g_{\omega\pi\gamma} \approx 0.322$; $g_{\omega NN} \approx 15.9$; $R_\omega \approx (0.155 - 0.127\, i)$

B Pseudo-scalar pole contribution to $(g-2)_\mu$

The purpose of this appendix is to explain some results relating to the pion pole contribution and workings of the code used in the hadronic light by light calculations. The requirements to run the code are:

- C++
- CERN Root
- GSL
- Make

B.1 Background

Our ultimate goal is to calculate the pseudoscalar pion-pole contribution $a_\mu^{\mathrm{HLbL}:\pi^0}$, which can be found through the following equation:

$$a_\mu^{\mathrm{HLbL}:\pi^0} = \left(\frac{\alpha}{\pi}\right)\left[a_\mu^{\mathrm{HLbL}:\pi^0(1)} + a_\mu^{\mathrm{HLbL}:\pi^0(2)}\right]$$

where α is the fine structure constant. The two terms on the right both have triple integral representations:

$$a_\mu^{\mathrm{HLbL}:\pi^0(1)} = \int_0^\infty dQ_1 \int_0^\infty dQ_2 \int_{-1}^1 d\tau w_1(Q_1,Q_2,\tau)\mathcal{F}_{\pi^0\gamma^*\gamma^*}(-Q_1^2,-(Q_1+Q_2)^2)\mathcal{F}_{\pi^0\gamma^*\gamma^*}(-Q_2^2,0) \tag{12}$$

$$a_\mu^{\mathrm{HLbL}:\pi^0(2)} = \int_0^\infty dQ_1 \int_0^\infty dQ_2 \int_{-1}^1 d\tau w_2(Q_1,Q_2,\tau)\mathcal{F}_{\pi^0\gamma^*\gamma^*}(-Q_1^2,-Q_2^2)\mathcal{F}_{\pi^0\gamma^*\gamma^*}(-(Q_1+Q_2)^2,0) \tag{13}$$

where w_1 and w_2 are weighting functions:

$$w_1(Q_1,Q_2,\tau) = \left(\frac{-2\pi}{3}\right)\sqrt{1-\tau^2}\frac{Q_1^3Q_2^3}{Q_2^2+m_\pi^2}I_1(Q_1,Q_2,\tau)$$

$$w_2(Q_1,Q_2,\tau) = \left(\frac{-2\pi}{3}\right)\sqrt{1-\tau^2}\frac{Q_1^3Q_2^3}{(Q_1+Q_2)^2+m_\pi^2}I_2(Q_1,Q_2,\tau)$$

The definitions of I_1 and I_2 are quite complex, so they are omitted for now. Their exact definitions can be found in the equation appendix at the end of this document, as well as a table of all relevant constants.

The following figure contains plots of the weighting functions with various fixed values of Q_1 and Q_2 while varying τ (note that the y-axis on the right plot is logarithmic):

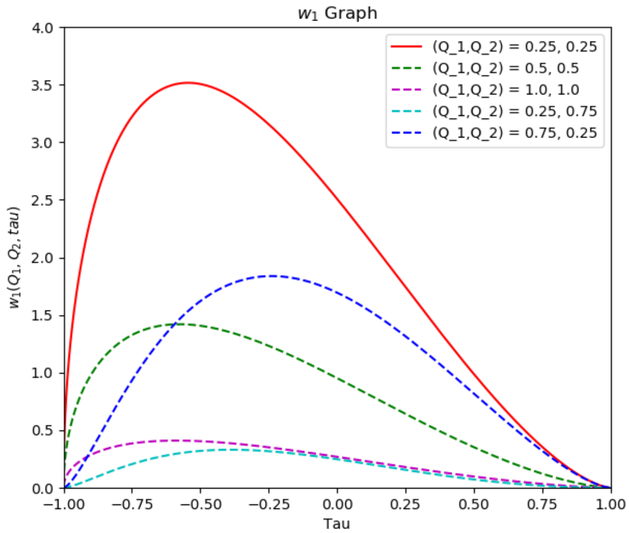

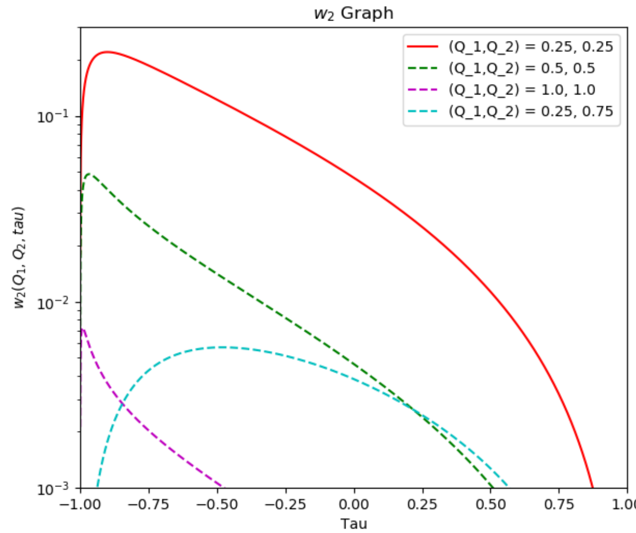

The integrals also involve the on-shell transition form factor for the pion. In particular, we need the lowest meson dominance plus vector parameterization, or LMD+V form factor:

$$\mathcal{F}^{\mathrm{LMD+V}}_{\pi^0\gamma^*\gamma^*}(q_1^2, q_2^2) = \frac{F_\pi}{3} \frac{q_1^2 q_2^2 (q_1^2 + q_2^2) + h_2 q_1^2 q_2^2 + h_5 q_1^2 q_2^2 + h_5 (q_1^2 + q_2^2) + h_7}{(q_1^2 - M_{V_1}^2)(q_1^2 - M_{V_2}^2)(q_2^2 - M_{V_1}^2)(q_2^2 - M_{V_2}^2)} \tag{14}$$

Descriptions of all relevant constants can be found at the end of the document.

B.2 Pion-Pole Contribution Calculations

In order to calculate the pion pole contribution, we must first compute two triple integrals. Of course, it would be impossible to do this by hand given the complexity of the integrands, so we resort to numerical methods. The standard Riemann sum or trapezoid rule algorithms are not be the best course of action however, since as the number of dimensions d in an integral increases they run in $\mathcal{O}(n^d)$. A better algorithm would be Monte Carlo integration, which runs in $\mathcal{O}(n)$ regardless of the number of dimensions, making it well-suited for high-dimensional integrals. Monte Carlo integration works by evaluating the integrand at random points in the domain of integration in order to compute the average value of the function over the domain. This number is then multiplied by the "volume" of the domain of integration to produce the final result. A naive algorithm uses uniform sampling over the whole domain, while more sophisticated algorithms such as MISER and VEGAS use stratified and importance sampling to place samples in areas which decrease the overall variance of the result.

Although the upper bounds of integration on Q_1 and Q_2 are both ∞, we do not need to integrate out this far in practice to get an accurate result. Both of the weighting functions approach 0 as $Q_1, Q_2 \to \infty$, so a much smaller upper bound of 20 can be used.

For implementation, GSL provides many optimized Monte Carlo integration algorithms in C++. Using the VEGAS algorithm with 40 million samples and a momentum cutoff of 20, we obtain the result

$$a_{\mu:\mathrm{LMD+V}}^{\mathrm{HLbL}:\pi^0} = 62.9201422692142 \times 10^{-11}$$

which agrees with the value calculated by Nyffeler of 62.9×10^{-11}.

B.3 Low Momentum Expansion

Another topic of interest is the low momentum form factor expansion, which approximates the LMD+V form factor for sufficiently small Q_1 and Q_2. The Q^6 expansion is:

$$\begin{aligned}\mathcal{F}_{Q^6}(-Q_1^2, -Q_2^2) = \frac{1}{4\pi^2 F_\pi}\big[1 - a(Q_1^2 + Q_2^2) + b(Q_1^4 + Q_2^4) + cQ_1^2 Q_2^2 \\ +d(Q_1^6 + Q_2^6) + e(Q_1^4 Q_2^2 + Q_1^2 Q_2^4) + \cdots\big]\end{aligned} \tag{15}$$

This expansion is valid in the region $Q_1^2 < 0.1,\ Q_2^2 < 0.1$. Below is a graph of the LMD+V form factor along with the Q^4 and Q^6 expansions.

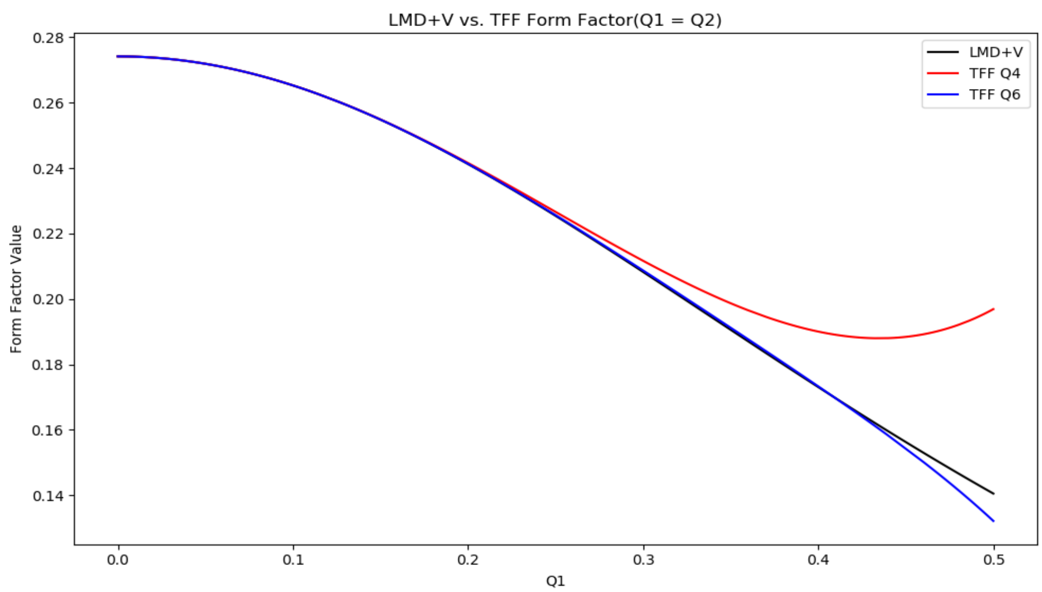

The two expansions are quite accurate in low momentum regions. We can obtain a measure of how accurate they are by performing the integrals in equations (1) and (2) and calculating $a_\mu^{\mathrm{HLbL}:\pi^0}$ using a small momentum cutoff of $Q_{1,2} < 0.1$. The following result used 40 million samples per integral:

```
Integration to Q < 0.1 with 40,000,000 samples
Integral 1 (LMD+V):     0.001005460894  Sigma: 1.864345197e-08
Integral 2 (LMD+V):     0.0001717746828 Sigma: 4.577028494e-09

Integral 1 (Q4)   :     0.001005481982  Sigma: 1.832570684e-08
Integral 2 (Q4)   :     0.000171768857  Sigma: 4.722432529e-09

Integral 1 (Q6)   :     0.001005465541  Sigma: 1.846705857e-08
Integral 2 (Q6)   :     0.0001717705784 Sigma: 4.358205314e-09

Final LMD+V       :     1.475399897e-11
Final Q4          :     1.475419025e-11
Final Q6          :     1.475400577e-11


% Error Q4 = 0.001296464429
% Error Q6 = 4.605865611e-05
```

The percent error is extremely small, so we can be confident that these expansions accurately model the LMD+V form factor. Even when we integrate out to the $Q < 0.55$ region, the Q^6 expasion is still reasonably accurate:

```
Integration to Q < 0.55 with 40,000,000 samples
Integral 1 (LMD+V):     0.03059591231   Sigma: 1.143014661e-06
Integral 2 (LMD+V):     0.001228622807  Sigma: 7.092076856e-08

Integral 1 (Q4)   :     0.03445752339   Sigma: 1.29445538e-06
Integral 2 (Q4)   :     0.001255706317  Sigma: 7.560896752e-08

Integral 1 (Q6)   :     0.0292823835    Sigma: 1.31088181e-06
Integral 2 (Q6)   :     0.001222610122  Sigma: 7.34236183e-08

Final LMD+V       :     3.98848937e-10
Final Q4          :     4.475849735e-10
Final Q6          :     3.823114535e-10


% Error Q4 = 12.21917171
% Error Q6 = 4.146302504
```

Additionally, we are interested in the parameters a, b, c, d, e, and the constant $\Gamma_{\pi^0 \to \gamma\gamma'}$. We can find the uncertainty in these values by calculating the partial derivatives of the pseudoscalar pion pole contribution $a_\mu^{\text{HLbL};\pi^0}$ with respect to each parameter. We can do this by by using the standard two-sided finite difference algorithm for derivatives:

Let $f : \mathbb{R}^6 \to \mathbb{R}$ be a function that takes the parameters $a, b, c, d, e, \Gamma_{\pi^0 \to \gamma\gamma'}$ as input and outputs the value of the pseudoscalar pion pole contribution using the Q^6 form factor expansion. If we wanted to find the uncertainty in a, for example, we would need to calculate $\dfrac{\partial f}{\partial a}$, which using the two-sided finite differnce is:

$$\frac{\partial f}{\partial a} \approx \frac{f\big(a(1+p), b, c, d, e, \Gamma\big) - f\big(a(1-p), b, c, d, e, \Gamma\big)}{2ap}$$

where $0 < p << 1$ is some small percent offset. In this case, we would choose all parameter values to be their mean value, as in the table of constants. Ideally we want p to be as small as possible, but due to the limitations of floating point arithmetic if p is too small we introduce floating point errors into the calculation. On the other hand, if p is too large the approximation of the partial derivative becomes less valid. In an attempt to mitigate these errors, we will calculate the partials for each parameter for a range of percent offsets and compare them to see if they agree. We find:

```
Integration up to Q < 0.32 with 10,000,000 samples

Partials - parameters varied by 0.25%
a     :       -3.3649414139212751e-11
b     :       6.5597577850400077e-13
c     :       7.5336493834179759e-13
d     :       -2.2389899845111552e-14
e     :       -2.5921871988282577e-13
gamma :       0.028048597506709651

Partials - parameters varied by 0.5%
a     :       -3.4449383778532745e-11
b     :       3.4142804377747982e-12
c     :       8.8450944603176724e-13
d     :       2.8415787365649684e-15
e     :       -9.0179242866092002e-14
gamma :       0.028048597506709985
```

```
Partials - parameters varied by 0.75%
a     :       -3.3191362216371211e-11
b     :       2.5755926746937237e-12
c     :       8.9698494346664814e-13
d     :       5.5273532206700047e-13
e     :       1.1963893088477835e-13
gamma :       0.028048597506711213

Partials - parameters varied by 1%
a     :       -3.2643828344676348e-11
b     :       2.7937088821432139e-12
c     :       7.6711187905363668e-13
d     :       2.4753257230670531e-13
e     :       3.3237715190804097e-14
gamma :       0.028048597506710987

Partials - parameters varied by 2%
a     :       -3.3252659401737983e-11
b     :       2.5268070693977975e-12
c     :       8.0415729114617521e-13
d     :       6.3470922586978126e-14
e     :       3.0352326917181194e-14
gamma :       0.028048597506710987
```

We see that the parameters a, b, and Γ have good agreement, while c, d, and e have less agreement. Increasing the integration bound to $Q < 0.55$ results in better agreement among all parameters:

```
Integration up to Q < 0.55 with 10,000,000 samples

Partials - parameters varied by 0.5%
a       :       -1.64032569337445e-10
b       :       3.38827807205793e-11
c       :       1.14428571606979e-11
d       :       9.08712120200189e-12
e       :       4.35623158169835e-12
gamma   :       0.0494522072073776

Partials - parameters varied by 1%
a       :       -1.64967438673216e-10
b       :       3.24854023731518e-11
c       :       1.1522291345106e-11
```

```
d       :       9.46112561685376e-12
e       :       3.93324334449662e-12
gamma   :       0.0494522072073796

Partials - parameters varied by 2%
a       :       -1.63683649020039e-10
b       :       3.33407981304216e-11
c       :       1.26548343516877e-11
d       :       9.09222852041125e-12
e       :       4.04912057232516e-12
gamma   :       0.0494522072073795
```

B.4 Code Documentation

The subsections here detail what each file does as well as how to compile and run them. The files themselves are also documented with comments in the code. There are 5 files in total:

- functions.h
- main.cpp
- error.cpp
- propagate.cpp
- Makefile

B.4.1 functions.h

This file defines the functions and physical constants needed in the HLbL calculation. Such functions include the form factors and weighting functions.

B.4.2 main.cpp

This program calculates the value $a_\mu^{\mathrm{HLbL};\pi^0}$. It does this using the VEGAS Monte Carlo integration algorithm (implemented by GSL) to calculate the relevant integrals.

B.4.3 error.cpp

This program calculates the percentage error of the Q^4 and Q^6 form factor expansions. The upper integration bounds on Q_1 and Q_2 can be changed by altering the value of the `limit` variable, and the number of samples used in the integration algorithm can be changed with the `calls` variable. Since a total of 6 integrals need to be calculated, the MISER algorithm (implemented in GSL) is used because it is faster than the VEGAS algorithm.

B.4.4 propagate.cpp

This program computes the partial derivatives of $a_\mu^{\mathrm{HLbL};\pi^0}$ with respect to the parameters a, b, c, d, e, and Γ using the Q^6 expansion. The MISER algorithm is used here since many integrals need to be calculated. The number of samples can be changed by changing the `samples` variable, and the integration bound can be changed with the `cutoff` variable.

B.4.5 Compiling and Running

To compile all of the code, simply run the command `make` in the same directory as the Makefile using the command line. This should generate several files. The important ones are `main`, `error`, and `propagate` (note that these files don't have extensions since they are executables). To run the relevant program, type `./<fileName>` into the command line. For example, to run `main.cpp`, type `./main` into the command line. To remove all of the generated files, run `make clean`. This will not affect any of the source files.

B.5 Weighting functions and form factors

The functions involved in the calculations are quite complicated, so the details are provided here.

B.5.1 Weighting Functions

$$w_1(Q_1, Q_2, \tau) = \left(\frac{-2\pi}{3}\right)\sqrt{1-\tau^2}\,\frac{Q_1^3 Q_2^3}{Q_2^2 + m_\pi^2} I_1(Q_1, Q_2, \tau)$$

$$w_2(Q_1, Q_2, \tau) = \left(\frac{-2\pi}{3}\right)\sqrt{1-\tau^2}\,\frac{Q_1^3 Q_2^3}{(Q_1+Q_2)^2 + m_\pi^2} I_2(Q_1, Q_2, \tau)$$

$$\begin{aligned} I_1(Q_1, Q_2, \tau) = X(Q_1, Q_2, \tau)\big[&8P_1P_2(Q_1\cdot Q_2) - 2P_1P_3(Q_2^4/m_\mu^2 - 2Q_2^2) + 4P_2P_3Q_1^2 - 4P_2 \\ &-2P_1(2 - Q_2^2/m_\mu^2 + 2(Q_1\cdot Q_2)/m_\mu^2) - 2P_3(4 + Q_1^2/m_\mu^2 - 2Q_2^2/m_\mu^2) + 2/m_\mu^2\big] \\ &-2P_1P_2(1 + (1-R_{m1})(Q_1\cdot Q_2)/m_\mu^2) + P_1P_3(2 - (1-R_{m1})Q_2^2/m_\mu^2) \\ &+P_2P_3(2 + (1-R_{m1})^2(Q_1\cdot Q_2)/m_\mu^2) + P_1(1-R_{m1})/m_\mu^2 + 3P_3(1-R_{m1})/m_\mu^2 \end{aligned}$$

$$\begin{aligned} I_2(Q_1, Q_2, \tau) = X(Q_1, Q_2, \tau)\big[&4P_1P_2(Q_1\cdot Q_2) + 2P_1P_3Q_2^2 - 2P_1 + 2P_2P_3Q_1^2 - 2P_2 - 4P_3 - 4/m_\mu^2\big] \\ &-2P_1P_2 - 3P_1(1-R_{m2})/(2m_\mu^2) - 3P_2(1-R_{m1})/(2m_\mu^2) - P_3(2 - R_{m1} - R_{m2})/(2m_\mu^2) \\ &+P_1P_3(2 + 3(1-R_{m2})Q_2^2/(2m_\mu^2) + (1-R_{m2})^2(Q_1\cdot Q_2)/(2m_\mu^2)) \\ &+P_2P_3(2 + 3(1-R_{m1})Q_1^2/(2m_\mu^2) + (1-R_{m1})^2(Q_1\cdot Q_2)/(2m_\mu^2)) \end{aligned}$$

$$Q_3^2 = Q_1^2 + 2Q_1 \cdot Q_2 + Q_2^2$$
$$Q_1 \cdot Q_2 = Q_1 Q_2 \tau$$

$$P_i = \frac{1}{Q_i^2},\ i = 1, 2, 3$$

$$X(Q_1, Q_2, \tau) = \frac{1}{Q_1 Q_2 x} \arctan\left(\frac{zx}{1 - z\tau}\right)$$
$$x = \sqrt{1 - \tau^2}$$
$$z = \frac{Q_1 Q_2}{4m_\mu^2}(1 - R_{m1})(1 - R_{m2})$$
$$R_{mi} = \sqrt{1 + \frac{4m_\mu^2}{Q_i^2}},\ i = 1, 2$$

B.5.2 Form Factors

$$\mathcal{F}_{\pi^0\gamma^*\gamma^*}^{\mathrm{LMD+V}}(q_1^2, q_2^2) = \frac{F_\pi}{3} \frac{q_1^2 q_2^2 (q_1^2 + q_2^2) + h_2 q_1^2 q_2^2 + h_5 (q_1^2 + q_2^2) + h_7}{(q_1^2 - M_{V_1}^2)(q_1^2 - M_{V_2}^2)(q_2^2 - M_{V_1}^2)(q_2^2 - M_{V_2}^2)}$$

$$\mathcal{F}_{Q^4}(-Q_1^2, -Q_2^2) = \sqrt{\frac{4\Gamma_{\pi^0\to\gamma\gamma'}}{\pi\alpha^2 m_\pi^3}} \left[1 - a(Q_1^2 + Q_2^2) + b(Q_1^4 + Q_2^4) + cQ_1^2 Q_2^2 + \cdots\right]$$

$$\mathcal{F}_{Q^6}(-Q_1^2, -Q_2^2) = \sqrt{\frac{4\Gamma_{\pi^0\to\gamma\gamma'}}{\pi\alpha^2 m_\pi^3}} \left[1 - a(Q_1^2 + Q_2^2) + b(Q_1^4 + Q_2^4) + cQ_1^2 Q_2^2 + d(Q_1^6 + Q_2^6) + e(Q_1^4 Q_2^2 + Q_1^2 Q_2^4) + \cdots\right]$$

B.6 Constants

Name	Symbol	Value	Units
Fine Structure Constant	α	0.0072973525693	-
Pion Mass	m_π	0.1349768	GeV/c^2
Muon Mass	m_μ	0.1056583745	GeV/c^2
Pion Decay Constant	F_π	0.0924	GeV
Vector Meson Mass 1	M_{V_1}	0.77549	GeV
Vector Meson Mass 2	M_{V_2}	1.465	GeV
LMD+V Parameter 1	h_2	-10.634883404844444	GeV^2
LMD+V Parameter 2	h_5	6.93	GeV^4
LMD+V Parameter 3	h_7	-14.827668978756119	GeV^6
TFF Expansion Param 1	a	1.6613939123981294*	GeV^{-2}
TFF Expansion Param 2	b	2.7619453491551749*	GeV^{-4}
TFF Expansion Param 3	c	3.259027816403921*	GeV^{-6}
TFF Expansion Param 4	d	-4.59258	GeV^{-6}
TFF Expansion Param 5	e	-5.58268	GeV^{-6}
?	Γ and $\Gamma_{\pi^0\to\gamma\gamma'}$	7.7291993×10^{-9}	GeV

$*$ - The values for the parameters a, b, and c in the table are approximate. Their exact forms are:

$$a = \frac{1}{M_{V_1}^2} + \frac{1}{M_{V_2}^2} + \frac{h_5}{h_7}$$

$$b = \frac{1}{M_{V_1}^4} + \frac{1}{M_{V_2}^4} + \frac{1}{M_{V_1}^2 M_{V_2}^2} + \frac{h_5}{h_7}\left(\frac{1}{M_{V_1}^2} + \frac{1}{M_{V_2}^2}\right)$$

$$c = \left(\frac{1}{M_{V_1}^2} + \frac{1}{M_{V_2}^2}\right)^2 + \frac{h_2}{h_7} + 2\frac{h_5}{h_7}\left(\frac{1}{M_{V_1}^2} + \frac{1}{M_{V_2}^2}\right)$$

References

[1] I. Larin et al. Precision measurement of the neutral pion lifetime. *Science*, 368:5064–509, 2020.

[2] A. M. Bernstein and B. R. Holstein. *Rev. Mod. Phys.*, 85:49, 2013.

[3] M. Vanderhaeghen I. Danilkin, C.F. Redmer. The hadronic light-by-light contribution to the muon's amomalous magnetic moment. *Prog. Part. Nucl. Phys.*, 107:20, 2019.

[4] T. Aoyama et al. The anomalous magnetic moment of the muon in the Standard Model. *Phys. Rep.*, 887:1, 2020.

[5] E. Hadjimichael and S. Fallieros. *Phys. Rev. C*, 39:1438, 1989.

[6] A. Bramon J. Bijnens and F. Cornet. *Phys. Rev. Lett.*, 61:1453, 1988.

[7] B. Moussallam. *Phys. Rev. D*, 51:4939, 1995.

[8] A. Bramon J. Bijnens and F. Cornet. *Z. Phys. C*, 46:599, 1990.

[9] L.G. Landsberg. *Phys. Rep.*, 128:302, 1985.

[10] P. Maris and P.C. Tandy. *Nuclear Physics A*, 663 & 664:401c, 2000.

[11] M.R. Frank et al. *Phys. Lett. B*, 359:17, 1995.

[12] T. Blum et al. Hadronic Light-by-Light Scattering Contribution to the Muon Anomalous Magnetic Moment from Lattice QCD. *Phys. Rev. Lett.*, 124:132002, 2020.

[13] En-Hung Chao et al. Hadronic light-by-light contribution to $(g-2)_\mu$ from lattice QCD: a complete calculation. *EPJC*, 81:651, 2021.

[14] *The Science Driving the 12 GeV Upgrade of CEBAF, https://www.jlab.org/div dept/physics division/GeV/WhitePaper V11.pdf*, 2001.

[15] *Conceptual Design Report (CDR) for the Science and Experimental Equipment for the 12 GeV Upgrade of CEBAF, https://www.jlab.org/div dept/physics division/GeV/doe_review/CDR for Science Review.pdf*, 2005.

[16] B. Abi et al. Measurement of the Positive Muon Anomalous Magnetic Moment to 0.46 ppm. *Phys. Rev. Lett.*, 126:141801, 2021.

[17] A. Nyffeler. Precision of a data-driven estimate of hadronic light-by-light scattering in the muon g-2: Pseudoscalar-pole contribution. *Phys. Rev. D*, 94:053006, 2016.

[18] H. J. Behrend et al. (CELLO Collaboration). *Z. Phys. C*, 49:401, 1991.

[19] J. Gronberg et al.(CLEO Collaboration). *Phys. Rev. D*, 57:33, 1998.

[20] C.F. Redmer (BESIII Collaboration). *13th Conference on the Intersections of Particle and Nuclear Physics*, 2018.

[21] Lazzeroni et al. *Phys. Lett. B*, 768:38, 2017.

[22] P. Adlarson (A2 Collaboration). *Phys. Rev. C*, 95:035208, 2017.

[23] R. Akhmetshin (CMD-2 Collaboration). *Phys. Lett. B*, 605:26, 2005.

[24] M. Achasov et al. *Phys. Lett. B*, 559:171, 2003.

[25] M. Achasov et al.(SND Collabortion). *Phys. Rev. D*, 93:092001, 2016.

[26] M. Achasov et al. *Phys. Rev. D*, 98:112001, 2018.

[27] S. Gevorkyan, I. Larin, R. Miskimen, and E. Smith. Photoproduction of pion pairs at high energy and small angles. *[arXiv:2201.09923 [nucl-th]]*, 1 2022.

[28] Fan Yang et al. *J. Phys.: Conf. Ser.*, 404:012025, 2012.

[29] S. Fegan et al. Assessing the performance under ionizing radiation of lead tungstate scintillators for EM calorimetry in the CLAS12 Forward Tagger. *NIM*, A789:101, 2015.

[30] I.Larin, A.Gasparian, S.Gevorkyan, L.Gan. The π^0 background from ω and ρ,mesons photoproduction in PrimEx. *PrimEx-II experiment note #51, https://www.jlab.org/primex/primex_notes/omega_note.pdf*, 2007.

[31] T. J. Brodbeck, P. Coddington, J. V. Morris, D. Newton, and T. Sloan. Photoproduction of omega Mesons from Complex Nuclei Targets. *Nucl. Phys. B*, 136:95–114, 1978.